CHARACTERIZATION OF RATE DEPENDENCY AND INHOMOGENEITY OF AORTIC TISSUE

A Dissertation
Submitted to
the Temple University Graduate Board

In Partial Fulfillment
of the Requirements for the Degree
DOCTOR OF PHILOSOPHY

---

by
Golriz Kermani
December 2016

Examining Committee Members:

Kurosh Darvish, Adviser	Department of Mechanical Engineering
Parsaoran Hutapea,	Department of Mechanical Engineering
Jie Yin,	Department of Mechanical Engineering
Michael Autieri, Reader	Physiology/CVRC, Lewis Katz School of Medicine

ABSTRACT

Traumatic aortic rupture (TAR) is one of the leading causes of morbidity and mortality in motor-vehicle accidents with the majority of injuries occurring in the peri-isthmus region. To date, the mechanisms of aorta injury are poorly understood as this injury cannot be replicated reliably in cadaver crash tests. Due to inconclusiveness of the experimental tests, finite element (FE) modeling is often used to gain a better insight into the mechanisms of TAR. However, the FE models are also hindered by many unknowns particularly the soft tissues biomechanical responses. A crucial step to improve the FE models of blunt chest trauma is to advance our understanding of the local mechanical properties of aortic tissue subject to high loading rates associated with TAR. The objective of this dissertation was to investigate the effects of tissue rate dependency and inhomogeneity in the modeling of loading conditions that lead to TAR.

The material properties of human aorta in large deformations and high loading rates were characterized based on oscillatory biaxial tests. It was shown that a quasilinear viscoelastic (QLV) model with the instantaneous elastic response of the second order and the reduced relaxation function with one exponentially decaying term could describe the experimental results between 20 Hz and 130 Hz. The obtained decay rates (in the range of 70 to 550 s^{-1}) were 10 to 100 folds higher than previously reported values and showed significant rate dependence within 10 ms after the loading. It was shown that the rate dependent properties, similar to the elastic properties, were anisotropic with generally

higher decay rate and stiffness observed in the circumferential direction compared to the longitudinal direction.

The inhomogeneity of porcine descending thoracic aorta was characterized in three dimensions using a nano-indentation technique and QLV modeling approach. The tests were conducted in the axial, circumferential, and radial orientations with about 100 μm spatial resolution. Aortic tissue was divided into 10 regions across the thickness, 4 quadrants in the circumferential direction, and 3 sections in the longitudinal direction. While across the thickness, the results in different orientations were significantly different, four distinct layers were identified that were matched with the anatomical features. In the axial direction, the medial quadrant, and in all directions, the proximal DTA had the lowest stiffness. The results predict that under equal stresses, the inner layers of the medial quadrant in upper DTA would undergo more strains and will be therefore more prone to failure. This prediction is in agreement with clinical observations.

The inhomogeneity and rate dependency of aorta were implemented in the Global Human Body Models Consortium full-body FE model. It was demonstrated that in a simulation of blunt chest impact, both features significantly affected the tissue strain levels particularly in the isthmus, arch, and ascending aorta. Accurate quantifications of these features are essential to assess the risk of aortic injury based on FE models.

To my parents, Soudabeh and Bahram,

and my brother, Maziar,

for their endless love, support, and inspiration.

ACKNOWLEDGMENTS

Success never happens in a vacuum, and I am humbly grateful to those that have enriched my journey to make possible this dissertation.

First, I would like to thank my advisor, Dr. Kurosh Darvish, for his never-ending guidance and support over the years. He has set an example of excellence as a researcher, mentor, and instructor, and been a role model for me. Thank you for everything, including all the life lessons, and great laughs as well - it's been a thrilling ride.

I would like to thank my dissertation committee members, Drs. Parsaoran Hutapea, Jie Yin, and Michael Autieri for their invaluable comments and feedback that enhanced the quality of my dissertation. I am grateful to Dr. Vallorie Peridier for all her support and the deep interest she showed in my academic success as well as personal development. You have been one of the bedrocks for my perseverance and dedication - thank you.

Thanks to my colleagues at Temple Biomechanics Laboratory. I particularly thank Dr. Ali Hemmasizadeh for providing the raw data of the nano-indentation tests that he conducted at the Biomechanics Lab.

A special shout-out to Sam for frequently forcing a smile upon unsavory times. And many thanks to Jacqueline, for her support and kindness - I am fortunate to have you.

I have been blessed with unyielding love, support, and encouragement from my parents, Soudabeh and Bahram. You are truly the best. And thanks to my brother and dearest friend, Maziar, who's always offered a shoulder to lean on, and a clear compass to learn from.

Golriz Kermani
July 2016

TABLE OF CONTENTS

LIST OF TABLES

LIST OF FIGURES

CHAPTER 1

INTRODUCTION

Traumatic Aortic Rupture (TAR) is the second most common cause of morbidity and mortality in motor vehicle accidents only after traumatic brain injury with survival rates of less than 10% in the field and less than 2% overall (Plummer et al., 2006; Richens, 2003). Consequently mitigation and prevention of TAR is of paramount importance. Despite the fact that safety devices, such as airbags and seat belts, are used extensively compared to the past; there are still many incidences of TAR in car crashes, particularly, in frontal crashes (Ryb et al., 2013).

TAR occurs generally in blunt chest trauma and is mostly observed at the isthmus, which is a transition region between the arch and the descending thoracic aorta (DTA). To date, aorta injury mechanisms are poorly understood as this injury is hard to reproduce in cadaver crash tests (Cavanaugh, 1993). Due to inconclusiveness of the experimental tests, finite element (FE) modeling is often used to gain a better insight into the mechanisms of TAR. With advancements in medical imaging techniques, the geometry of current FE models of human body for trauma applications (e.g., the GHBMC model) is highly accurate. However, TAR computational modeling is hindered by many unknowns in terms of the biomechanical properties of the materials and interfaces. For example, in the GHBMC model, the aorta is assumed to be homogeneous, isotropic, and linearly elastic while experimental results at the tissue level show that it is inhomogeneous, anisotropic, nonlinear, and viscoelastic (e.g., Mohan and Melvin, 1982; Shah et al., 2006). A

comprehensive knowledge of the biomechanical response of DTA to various loading conditions is essential for a better understanding of the mechanisms of injury and failure. Although the biomechanical characteristics of aortic tissue under physiological conditions have been investigated and modeled more extensively in the past, this information cannot be used in simulations of TAR, due to material nonlinearity and rate dependence. Meanwhile, the degree of aortic wall inhomogeneity and its effect on the risk of tissue failure under large deformations and high strain rates have not been investigated. Therefore, a crucial step to improve the FE models of chest trauma is to characterize the local biomechanical response of aortic tissue subject to high loading rates associated with TAR. This will be specifically useful in better elucidating the mechanisms of TAR, improving car safety and injury prevention considerations, and modeling clinical treatment of the injury.

The objective of this study was to test this hypothesis that the rate dependency and inhomogeneity of the aortic tissue significantly affect the evaluation of the risk of traumatic failure and/or injury. The content of the dissertation is structured as follows:

Chapter 2: Rate Dependency of Human Aortic Tissue from Oscillatory Biaxial Experiments in Sub-failure Deformations. This chapter reports the rate dependency of human DTA under large deformations obtained from oscillatory biaxial experiments. A quasi-linear viscoelastic (QLV) model is suggested and characterized for the nonlinear anisotropic rate dependency of human aortic tissue by analyzing the harmonics of oscillations with finite amplitude.

Chapter 3: Investigation of Inhomogeneous Material Behavior of Porcine Thoracic Aorta Using Nano-Indentation Tests. The results of nano-indentation tests on porcine DTA are presented. The elastic and relaxation properties are characterized using a QLV model, and changes in the anisotropic material properties in the radial, circumferential, and axial (longitudinal) directions are quantified in order to investigate the tissue inhomogeneity. The spatial resolution of the material properties is significantly increased compared to the previous works.

Chapter 4: Effect of Inhomogeneity and Rate Dependency of Aorta on the Prediction of Injury using GHBMC FBM. This chapter presents the results of the finite element (FE) simulation of dynamic chest impact tests using the Global Human Body Models Consortium (GHBMC) full-body model (FBM). Aorta tissue rate dependency and inhomogeneity that were characterized in the previous chapters were implemented in the model and their effects in changing the risk of TAR were evaluated.

Chapter 5 presents the concluding remarks and provides some directions for future research.

Appendix A discusses the foundations of the mathematical constraints used for optimizing the material coefficients in the biaxial oscillating tests. **Appendix B** provides more details about the nano-indentation experimental setup and test results. A brief description of the GHBMC model and the constitutive material models for thorax parts are given in **Appendix C**.

Chapters 2, 3 and 4 are written in the form of stand-alone journal papers. Chapter 3 has been already submitted and the other two will soon be submitted. The results

presented in this dissertation have been presented at several national conferences in the past years.

CHAPTER 2

RATE DEPENDENCY OF HUMAN AORTIC TISSUE FROM OSCILLATORY BIAXIAL EXPERIMENTS IN SUB-FAILURE DEFORMATIONS

Introduction

Characterizing the biomechanical behavior of arterial walls has been the focus of many studies in the past few decades due to their importance in understanding cardiovascular diseases, as the largest source of disease mortality in the United States (Alagona and Ahmad, 2015), and Traumatic Aortic Rupture (TAR), as one of the leading causes of fatal injuries observed in automotive accidents (Teixeira et al., 2011). TAR's poor survival rate, less than 10% in the field and less than 2% overall (Plummer et al., 2006; Richens, 2003), necessitates gaining a better understanding of aorta injury mechanisms and failure risk factors. A crucial step for this purpose is to characterize the biomechanical response of aortic tissue subject to high loading rates and large deformations associated with TAR. This will be specifically useful in developing more realistic finite element models of TAR, improving car safety and injury prevention considerations and modeling clinical treatments.

Aortic tissue, like most other soft tissues, exhibit viscoelasticity. However, its rate dependency of material properties at high loading rates that occur in TAR is poorly understood. While most of measurements of material properties have been conducted under physiologic conditions (e.g., Haskett et al., 2010; Kamenskiy et al., 2014), few studies have focused on high strain rates and large deformations. TAR mostly occurs in the peri-isthmus

region between the arch and the descending thoracic aorta (DTA) (Bertrand et al., 2008). The effect of strain rate on the failure properties of human DTA was studied using quasi-static and dynamic uniaxial (Mohan and Melvin, 1982) and inflation (biaxial) (Mohan and Melvin, 1983) tests. The uniaxial tests were conducted on small test coupons that were oriented in the longitudinal and circumferential directions. In both studies, it was observed that the failure stresses were larger at higher strain rates; however the failure extension ratios were not significantly affected by the strain rate or the tissue orientation. The main drawback of their study was that only one dynamic strain rate (about $80s^{-1}$) was applied. Shah et al. (2006) investigated the failure properties of human aortic samples from three different regions of the aorta, i.e., peri-isthmus, ascending, and descending, subject to equi-biaxial stretch loadings at two nominal extension rates of 1 m/s and 5 m/s. Although the corresponding Lagrangian strain rates were significantly different (77.86 ± 43.27 s^{-1} vs. 135.90 ± 55.34 s^{-1}), no significant difference was found in the material properties.

In the above-mentioned studies, no constitutive model was developed to describe the hyperelastic and viscoelastic behavior of the aortic tissue. Bass et al. (2001) used a 2-D Fung-type exponential hyperelastic model to describe the porcine aortic response to oscillating biaxial loading at nominal frequencies of 20 and 65 Hz. The data showed that the aortic behavior is dependent on the strain rate, with higher sensitivity in the circumferential direction.

It is evident that there is no consensus on the rate dependency of aortic tissue in the literature. Moreover, the hyperelastic constitutive models that are used often for arteries

such as Fung (Fung, 1993) and Holzapfel (Holzapfel et al., 2000) ignore the tissue rate dependent behavior altogether.

In this study, the rate dependence of the nonlinear dynamic response of human aortic tissue was investigated using oscillatory biaxial loading and applying a quasi-linear viscoelastic (QLV) model. The general form of the responses of the fully nonlinear and QLV models in oscillatory loading have been determined using multi-tone harmonic inputs (Darvish, 2009). This approach was used previously to characterize the nonlinear viscoelastic behavior of bovine brain tissue in oscillatory shear tests (Darvish and Crandall, 2001) and here, it is expanded to two dimensions.

Materials and Methods

Tissue Preparation and Testing

Six square shaped samples were obtained from six fresh human cadavers, all white (W), 4 men and 2 women, mean age of 56 years (26-75), from the peri-isthmus region. No arterial disease was reported in the donors' medical records and care was taken to extract homogeneous specimens with no visible plaques in the luminal side. The edges of the samples were cut along the circumferential (C) and the longitudinal (L) directions and the lengths at the zero-stress state (Z-state) was designated as L_C and L_L respectively. The tissue thickness at the Z-state was measured and represented by h. The specimens' specifications are listed in Table 1.

Table 1– General specifications of human aortic samples

Sample	Age	Gender (Race)	*Dimensions at Z-state (mm)*		
			L_C	L_L	h
1	75	M (W)	25.65	18.22	1.64
2	36	F (W)	24.15	21.51	1.51
3	63	F (W)	16.13	14.09	1.57
4	27	M (W)	20.34	17.67	1.36
5	70	M (W)	28.13	26.72	1.53
6	67	M (W)	19.79	16.23	1.65

Twelve to fourteen silk sutures (size 2-0 – approximately 0.3 mm in diameter) with about 50 cm length on each side were attached to four edges of the samples and were also used to mount the sample-suture assembly to the biaxial test setup including two pairs of electromagnetic shakers (VTS, Aurora, OH) and piezoresistive load cells (Model 31, Honeywell, Columbus, OH) (Figure 1). After the samples were pre-stretched, in-phase oscillatory biaxial tensile deformation was generated by the two shakers. Two frequencies of 20 Hz and 65 Hz were identified that yielded only in-plane deformations as they did not cause a natural frequency of the system. These frequencies were chosen for testing since their integer harmonics did not overlap. The acceleration of the shakers was measured with variable capacitance accelerometers (7290A, Endevco, San Juan Capistrano, CA) and the reaction forces in the load cells were recorded. For strain measurements, an array of small dots was marked on the lumen side of the specimens as photo targets for video motion analysis. Sample deformation was recorded from top view by a high-speed video camera (Kodak, Model RO) at 1000 fps. The details of the experimental setup is described further in Bass et al., (2001).

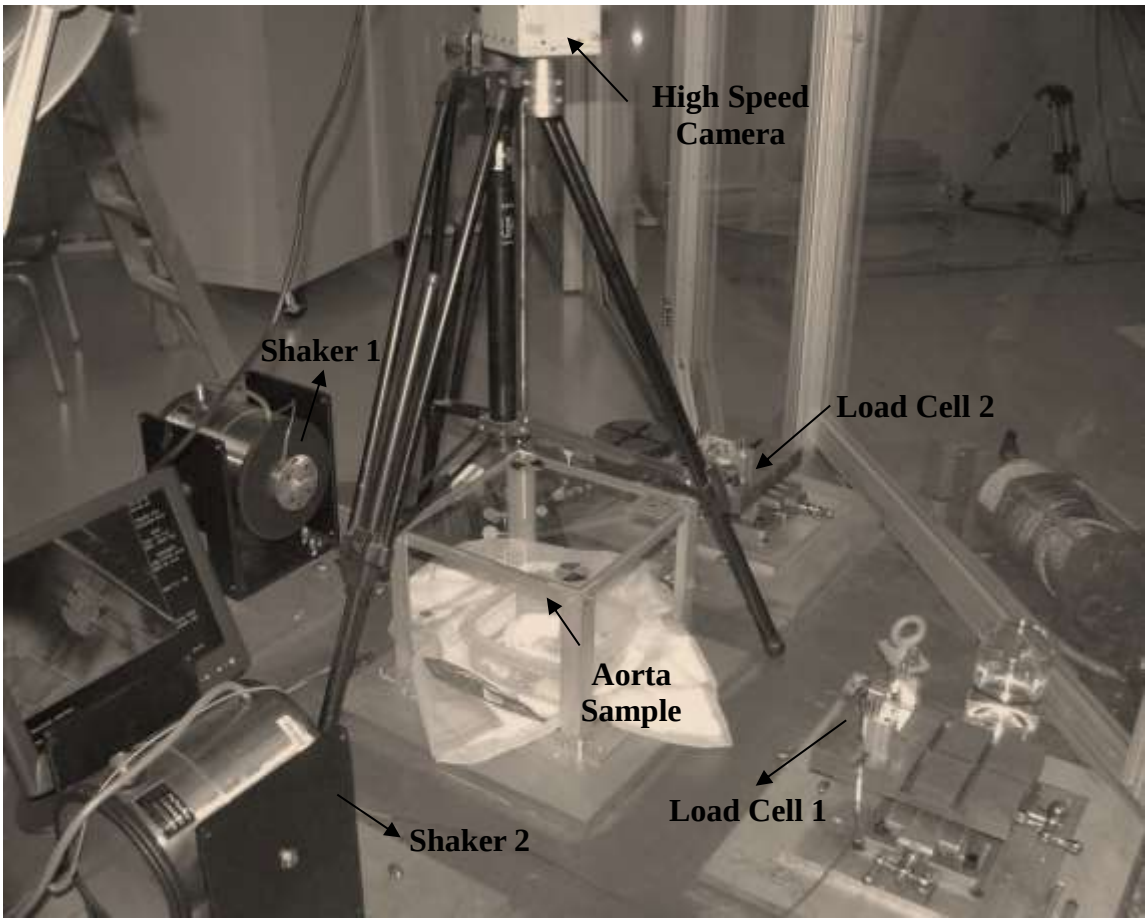

Figure 1– Biaxial testing setup showing two shaker-load cell pairs with the aorta sample mounted to them with silk sutures. The sample deformation is captured with the high-speed camera.

Strain and Stress Analysis

In order to characterize the mechanical properties of the aortic tissue, the stress and strain fields in the samples were calculated. For this purpose three states were considered (Figure 2): i) the zero stress state (*Z*-state) where no load was applied on the sample; ii) the state of initial static pre-stress (*I*-state) where the sample was pulled by adding 0.5N (51g)

weights from four sides to the end of each suture; and iii) the state of dynamic deformation state (*D*-state) where the sample was stretched in oscillatory motion in two perpendicular directions by the shakers. The preload (*I*-state) was applied so the sample would stay in tension during the *D*-state and it also stabilized the sample-sutures assembly by increasing its fundamental natural frequency and minimizing the off-plane vibrations. The initial strains and stresses in the specimens in the *I*-state were calculated and included in the subsequent data analysis. In the *I*-state, the taut sutures were secured to the shakers and load cells and the weights were removed.

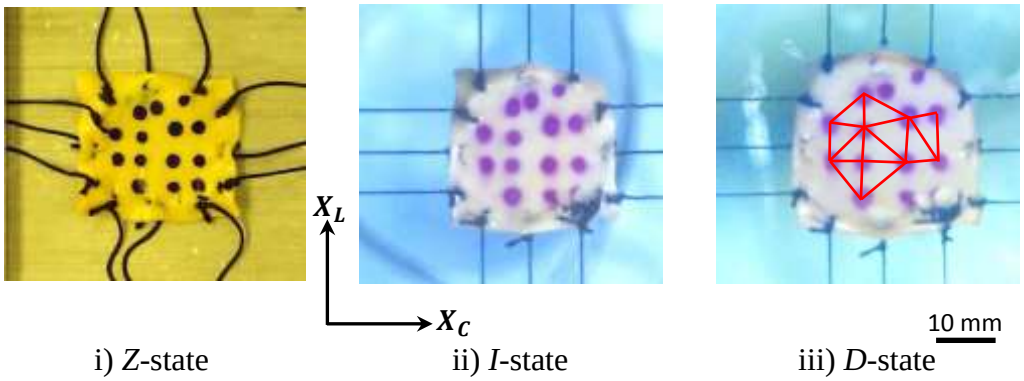

Figure 2– Three states of stress considered in the samples: i) zero stress state (*Z*-state), ii) initial static biaxial preload (*I*-state), and iii) dynamic biaxial loading (*D*-state). A view of the triangular mesh discretization is superimposed on the sample picture. (Sample 4) Dark dots were marked on the luminal surface of the specimens as photo targets to measure the biaxial strain.

The *Z*-state was considered as the reference configuration for a Lagrangian strain and stress analysis. This state was photographed using a digital camera and the distances

between the markers were measured using the Vision Assistant software (National Instruments, TX). From the images taken by the high-speed camera in the *I*- and *D*-states, the two-dimensional positions of the markers were calculated using an open-source MATLAB code (Hedrick, 2008) with about 0.1 mm accuracy. The *I*- and *D*-states shared the same coordinate system, which was designated as X_C-X_L with *C* and *L* representing the anatomical circumferential and longitudinal directions. Two deformation gradient tensors in two dimensions, $\mathbf{F}_{Z-I}$ and $\mathbf{F}_{I-D}$, were considered to quantify the deformations from *Z*-state to *I*- state, and from *I*-state to *D*-state, respectively. The overall deformation gradient was therefore $\mathbf{F}_{Z-D} = \mathbf{F}_{Z-I}\,\mathbf{F}_{I-D}$. For $\mathbf{F}_{Z-I}$, since equal weights were applied to the four edges, a pure biaxial stretch was assumed (diagonal terms equal to zero). For three vertices of a triangular element in the middle of the sample, *p*, *q*, and *r*, based on their distances in the *Z*-state ($\overline{pq}$ and $\overline{pr}$) and their coordinates in the *I*-state (p_C, p_L, and so on), the principal initial stretch ratios $\lambda_{C_I}$and λ_{L_I} were derived from the following equation (see Appendix A for the derivation):

$$\begin{bmatrix} 1/\lambda_{C_I}^2 \\ 1/\lambda_{L_I}^2 \end{bmatrix} = \begin{bmatrix} (p_C - q_C)^2 & (p_L - q_L)^2 \\ (p_C - r_C)^2 & (p_L - r_L)^2 \end{bmatrix}^{-1} \begin{bmatrix} \overline{pq}^2 \\ \overline{pr}^2 \end{bmatrix} \tag{2.1}$$

$\mathbf{F}_{Z-I}$ can therefore be written as:

$$\mathbf{F}_{Z-I} = \begin{bmatrix} \lambda_{C_I} & 0 \\ 0 & \lambda_{L_I} \end{bmatrix} \tag{2.2}$$

To calculate $\mathbf{F}_{I-D}$ for a triangular element (Figure 2-c), a linear biaxial displacement field was assumed between the *I*- and *D*-states:

$$u_i = a_{0i} + a_{1i}X_C + a_{2i}X_L \quad ; \quad i = C, L \tag{2.3}$$

where u_i is the displacement vector. Coefficients a_{ji} $(j = 0..2, i = C, L)$ were determined for each element and at each time step by solving Equation 2.3 for known values of nodal displacements and nodal coordinates obtained from the video data. The components of $\mathbf{F}_{I-D}$, based on Equation 2.3, can be written as:

$$\mathbf{F}_{I-D} = \begin{bmatrix} 1 + a_{1C} & a_{2C} \\ a_{1L} & 1 + a_{2L} \end{bmatrix} \tag{2.4}$$

It was verified that the diagonal terms in Equation 2.4 that describe the shear deformation were much smaller than a_{1C} and a_{2L}. The overall stretch ratios were therefore approximated as:

$$\lambda_C = \lambda_{CI}(1 + a_{1C}) \;\; ; \;\; \lambda_L = \lambda_{LI}(1 + a_{1L}) \tag{2.5}$$

The strain components were defined as:

$$\varepsilon_i = \lambda_i - 1 \;\; ; \;\; i = C, L \tag{2.6}$$

The components of the first Piola-Kirchhoff (engineering) stress tensor (**P**) were calculated as:

$$P_C = \frac{f_C}{L_L h} \;, \quad P_L = \frac{f_L}{L_C h} \tag{2.7}$$

where f_C and f_L are the forces measured by the load cells in the *C* and *L* directions, respectively. To describe the constitutive model of aorta, the components P_i were related to ε_i. These components satisfy the principle of objectivity for large deformations (Lai et al., 2004).

Constitutive Model

It is well known that the aortic tissue material behavior is nonlinear (e.g., Mohan and Melvin, 1983; Shah et al., 2006) and the method of oscillatory tests (forced vibration) allows for determining the degree of this nonlinearity directly without the need for relying solely on curve fitting. The harmonic distortions in the tissue force response were used for this purpose. The quantities used were the nth harmonic distortion (HD_n), which is the relative distortion of the first n harmonics with respect to the fundamental frequency ($HD_n = \frac{1}{A_1}(\sum_{i=2}^{n} A_i^2)^{0.5}$), and the total harmonic distortion (THD), which is the distortion from the harmonics plus noise in the spectrum ($THD = \frac{1}{A_1}(\sum(APS - DC - A_1))^{0.5}$. APS is the auto power spectrum of the signal, DC is the signal average values, and A_1 is the amplitude of the fundamental frequency. HD_n shows how much the response deviates from the linear response and THD shows that the deviation from linearity is random or it is because of nonlinearity in the system. When the acceleration input is linear, but showing that $THD \approx HD_2$, it can be concluded that the tissue nonlinearity is of the second order.

For simplicity, a QLV model was assumed to describe the tissue rate dependency. For oscillatory instantaneous elastic function, P_i^e, the Fourier Transform of the stress response can be written as:

$$\bar{P}_i(\omega) = i\omega\bar{G}(\omega)\bar{P}_i^e(\omega) \tag{2.8}$$

In the above equation, bar represents the Fourier Transform. $M(\omega) = i\omega\bar{G}(\omega)$ is the reduced complex modulus that is between 0 and 1 and makes the constitutive model frequency dependent. In the time domain, $G(t)$ is the reduced relaxation function, also

between 0 and 1, which in a QLV model is assumed to be independent of strain. For a second-order nonlinearity and ignoring the shear terms, P_i^e can be generally written as:

$$P_i^e = b_{1i}\varepsilon_C + b_{2i}\varepsilon_L + b_{3i}\varepsilon_C^2 + b_{4i}\varepsilon_L^2 + 2b_{5i}\varepsilon_C\varepsilon_L \quad ; \quad i = C, L \tag{2.9}$$

The 10 material coefficients, b_{ji} $(j = 1..5, i = C, L)$ are to be determined based on the experimental data.

Dynamic Material Characterization

In order to quantify $M(\omega)$ and b_{ji} from experimental data, the biaxial stress responses are obtained based on the in-phase biaxial strains. The strains are assumed to be single harmonic functions superimposed on constant (average) strains:

$$\varepsilon_i = \varepsilon_{i0} + A_i \sin(\omega_I t) \quad ; \quad i = C, L \tag{2.10}$$

where A_i and ω_I represent the input amplitudes and frequency, respectively. The biaxial stress response of the QLV model (up to the second order) was calculated by substituting equations (2.9) and (2.10) in the constitutive equation (2.8):

$$\begin{aligned} P_i(t) = &\Big(b_{1i}\varepsilon_{C0} + b_{2i}\varepsilon_{L0} + 2b_{5i}\varepsilon_{C0}\varepsilon_{L0} + b_{3i}\varepsilon_{C0}^2 + b_{4i}\varepsilon_{L0}^2 + b_{5i}A_CA_L + \\ &\tfrac{1}{2}(b_{3i}A_C^2 + b_{4i}A_L^2)\Big)M(0) + (b_{1i}A_C + b_{2i}A_L + 2(b_{5i}A_L + b_{3i}A_C)\varepsilon_{C0} + \\ &2(b_{5i}A_C + b_{4i}A_L)\varepsilon_{L0})M(\omega_I)\sin(\omega_I t) - \tfrac{1}{2}(b_{3i}A_C^2 + b_{4i}A_L^2 + \\ &2b_{5i}A_CA_L)M(2\omega_I)\cos(2\omega_I t) \quad ; \quad i = C, L \end{aligned} \tag{2.11}$$

As expected, the stress response contains additional terms in the zero frequency (average) and terms related to the second harmonic of the fundamental frequency, which are due to the nonlinearity of the material model. $M(\omega)$ represents the tissue rate dependent

behavior in the frequency range of 20 to 130 Hz that the material was tested and was written as a Kelvin-type model:

$$M(\omega) = i\omega\bar{G}(\omega) = \frac{i\omega G_1}{i\omega + \beta_1} + G_\infty \quad ; \quad (G_1 + G_\infty = 1) \tag{2.12}$$

in which β_1 is the decay rate and G_1 is the corresponding relaxation amplitude to be determined. G_∞ is the steady-state normalized amplitude. Since $M(\omega)$ is a complex number, it causes phase shits (positive for real materials) between the stress harmonics and strain.

Optimization Procedure

The objective of the material characterization was to find parameters G_1, β_1, and b_{ji}. Based on oscillatory loading of the sample, Fast Fourier Transform (FFT) of the stress and strain signals in the circumferential and longitudinal directions were calculated. First, the phase shifts, ϕ_i, between the stress and the corresponding strain signals were derived. Anisotropy of ϕ_i was evaluated but ignored for subsequent calculations and the average values in the two directions were used. By knowing ϕ_i in the two input frequencies (20 and 65 Hz), G_1 and β_1 were found exactly. The derived reduced complex modulus was used in Equation 2.11 and by comparing the model and experimental results for the amplitudes of *C* and *L* stresses at 0 Hz (average), the fundamental frequency, and the 2nd harmonic for the two input frequencies, a system of 12 equations were formed for the 10 unknowns b_{ji}. Additionally, two sets of constraints were considered for b_{ji}. The local stiffness matrix $\boldsymbol{C}$ of the instantaneous elastic response (Equation 2.9) can be written as:

$$\boldsymbol{C} = \begin{bmatrix} b_{1C} + 2b_{3C}\varepsilon_C + 2b_{5C}\varepsilon_L & b_{2C} + 2b_{4C}\varepsilon_L + 2b_{5C}\varepsilon_C \\ b_{1L} + 2b_{3L}\varepsilon_C + 2b_{5L}\varepsilon_L & b_{2L} + 2b_{4L}\varepsilon_L + 2b_{5L}\varepsilon_C \end{bmatrix} \quad (2.13)$$

One constraint was that $\boldsymbol{C}$ should be positive definite at all times, i.e., if local strain increases then stress should also increase (Holzapfel et al., 2000). Another was that the condition number of $\boldsymbol{C}$ ($k(\boldsymbol{C}) = \|\boldsymbol{C}\|\|\boldsymbol{C}^{-1}\|$, where $\|.\|$ is the second norm of the matrix) should be equal or less than 200. This ensured that $\boldsymbol{C}$ would be invertible and the compliance values would be meaningful (Sun and Sacks, 2005). These constraints, in addition to assuring that the elastic parameters are physically meaningful, are also necessary for numerical stability of computational models that utilize the constitutive Equation 2.9. Since the two constraints are functions of strain, they were written for the average, minimum and maximum values of strains and therefore, resulted in 6 constraint equations. The system 12 equations and 6 constraints with 10 unknowns was solved using the method of least-squares.

Results

Representative time histories of measured forces and accelerations and also calculated stresses and strains for the two directions and two frequencies are shown in Figure 3 and Figure 4, respectively. As can be seen, the accelerations of shakers were adjusted to achieve equal forces in the two directions. While the stresses were almost the same in the two directions, the strains were different due to material anisotropy. The initial pre-stretch to the *I*-state (Equation 2.2) was between 1.07 to 1.20 and 1.15 to 1.25, in the *C* and *L* directions, respectively. The shear strains were verified to be small with average

and standard deviation of 0.011 (0.008). Additionally, the uniformity of strains calculated for each triangular element in the middle of the sample was verified to be less than 5%.

Figure 5 summarizes the experimental stress versus strain results. Only one steady-state cycle is shown for clarity. While the stresses were kept fairly the same, significant inter-specimen variability was observed in the strains. Hysteresis loops and change in their slopes due to frequency indicated a rate dependent behavior. In most samples, as expected, the extension in the *C* direction was less than the *L* direction due to material anisotropy.

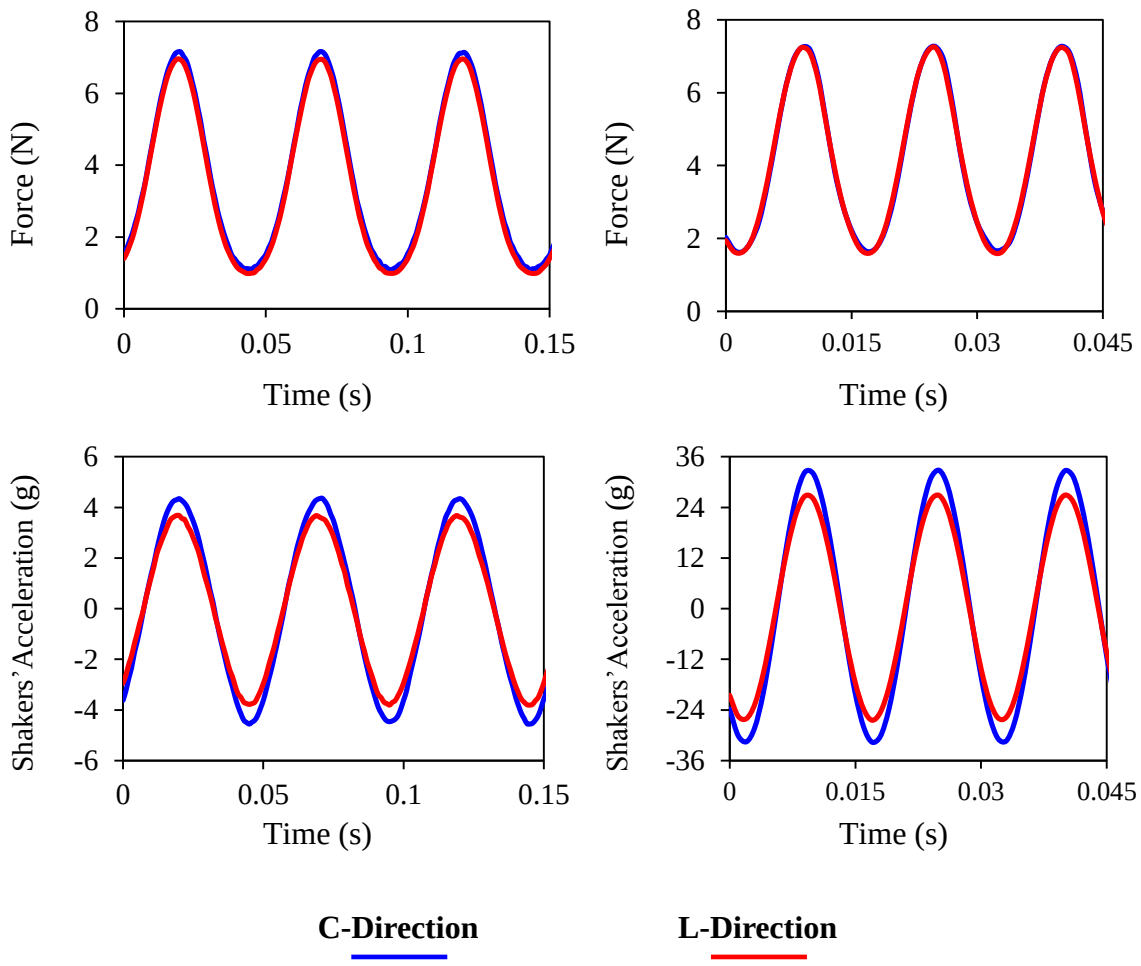

Figure 3– Representative (Sample 5) time histories of force (top row) and acceleration (bottom row) at 20 Hz (left column) and 65 Hz (right column).

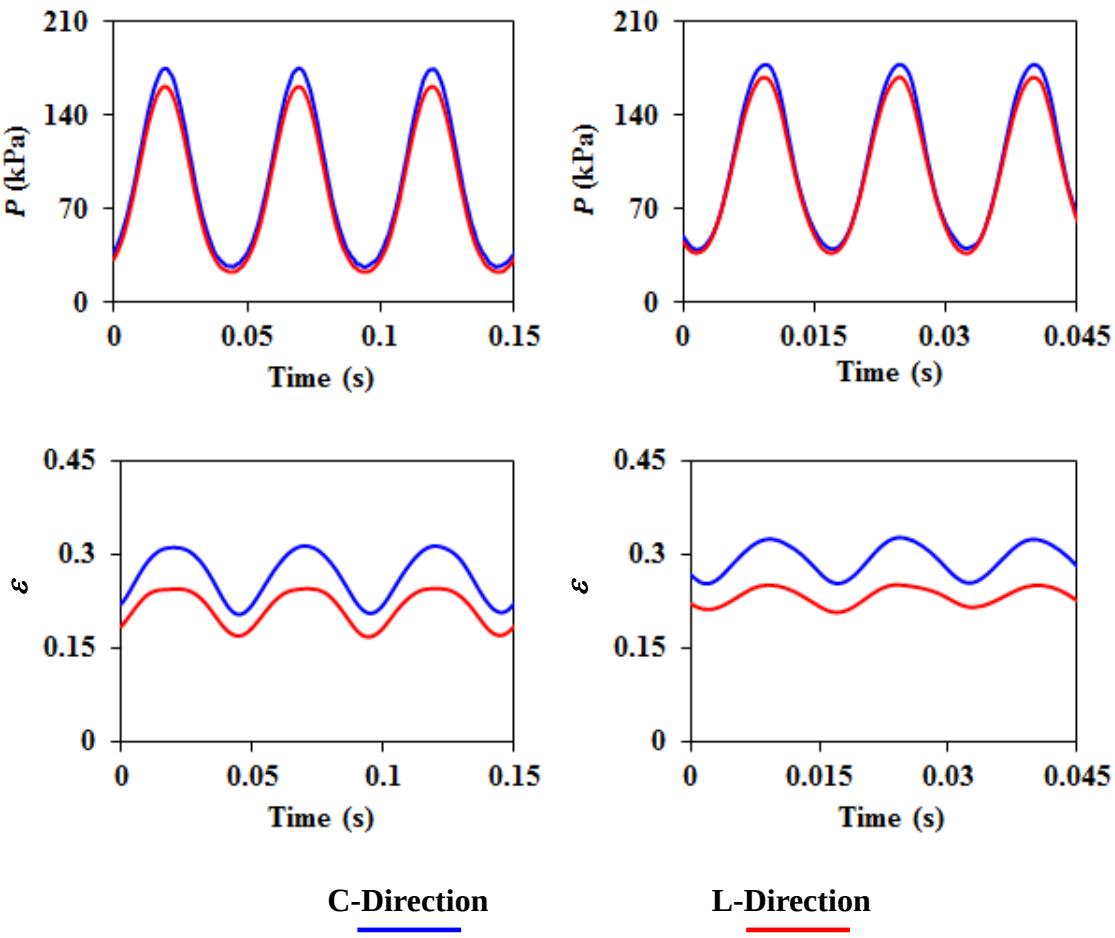

Figure 4– Representative (Sample 5) time histories of stress (top row) and strain (bottom row) at 20 Hz (left column) and 65 Hz (right column).

A representative spectra of force signals are shown in Figure 6 for the two directions and two frequencies, which show that the second-order harmonic was much higher than the third-order and other harmonics. Average values of *THD* and HD_2 of the force and acceleration signals are shown in Figure 7 (error bars represent the standard deviation). The figure shows that the distortion in force (output) was about 9 times the distortion in acceleration (input) indicating that the nonlinearity was primarily caused by

the material. Comparison between the HD_2 and *THD* of the force signal revealed that the second harmonic distortion has the main contribution to the total harmonic distortion, i.e., the nonlinearity in the system was primarily of the second order ("National Instruments," 1998). A two-tailed t-test analysis of HD_2 and *THD* showed that the nonlinearities observed in the two directions were the same (p = 0.89).

The optimized material parameters are listed in Table 2. For Sample 6, since no data at 65 Hz could be obtained due to connection failure, the material parameters were not calculated. The goodness of fit for each frequency in time domain is given by R^2 values. A representation of how the QLV model matched the experimental data is shown in Figure 8. As shown, the reduced complex modulus fitted the phase shift exactly and the elastic response captured the oscillatory response in the two directions and two frequencies satisfactorily (overall $R^2 = 0.83$).

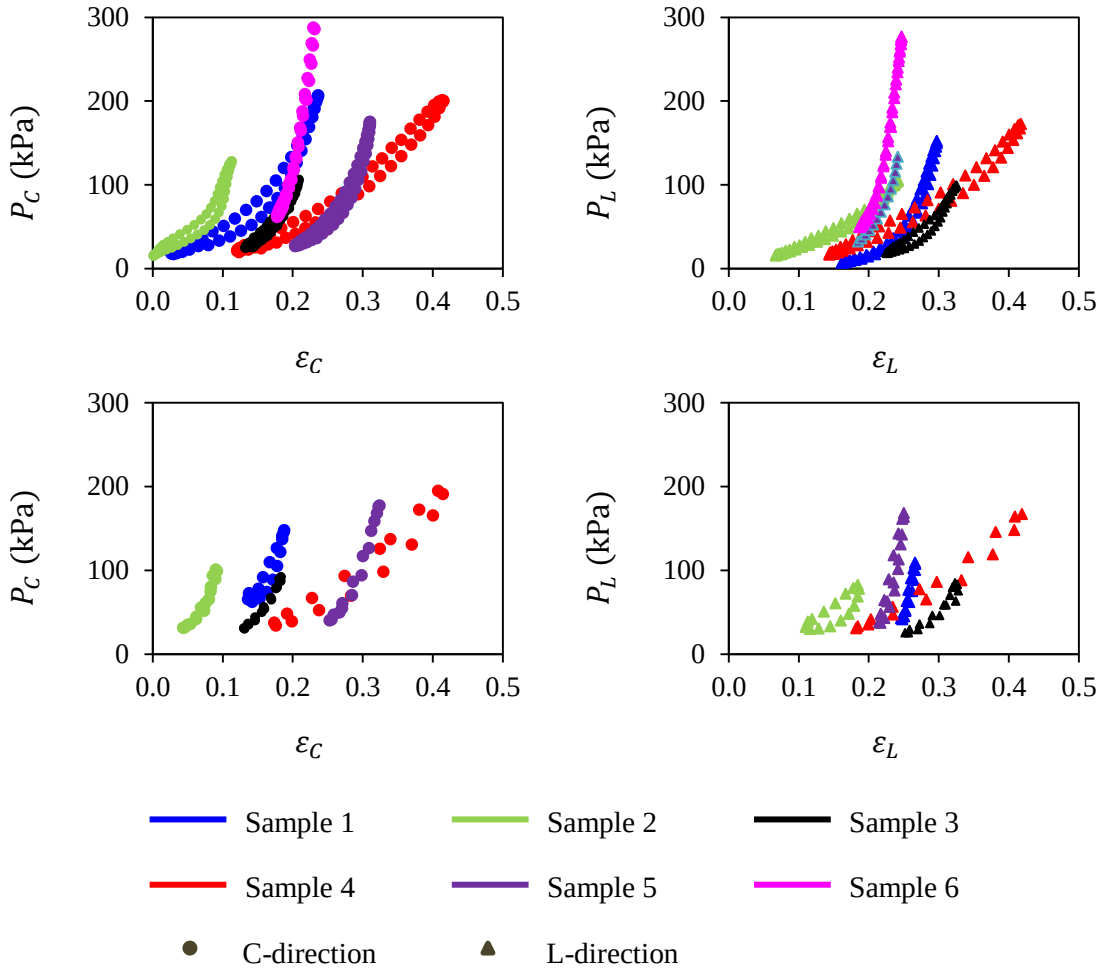

Figure 5– Experimental circumferential (left) and longitudinal (right) stress versus strain curves at 20 Hz (top) and 65 Hz (bottom).

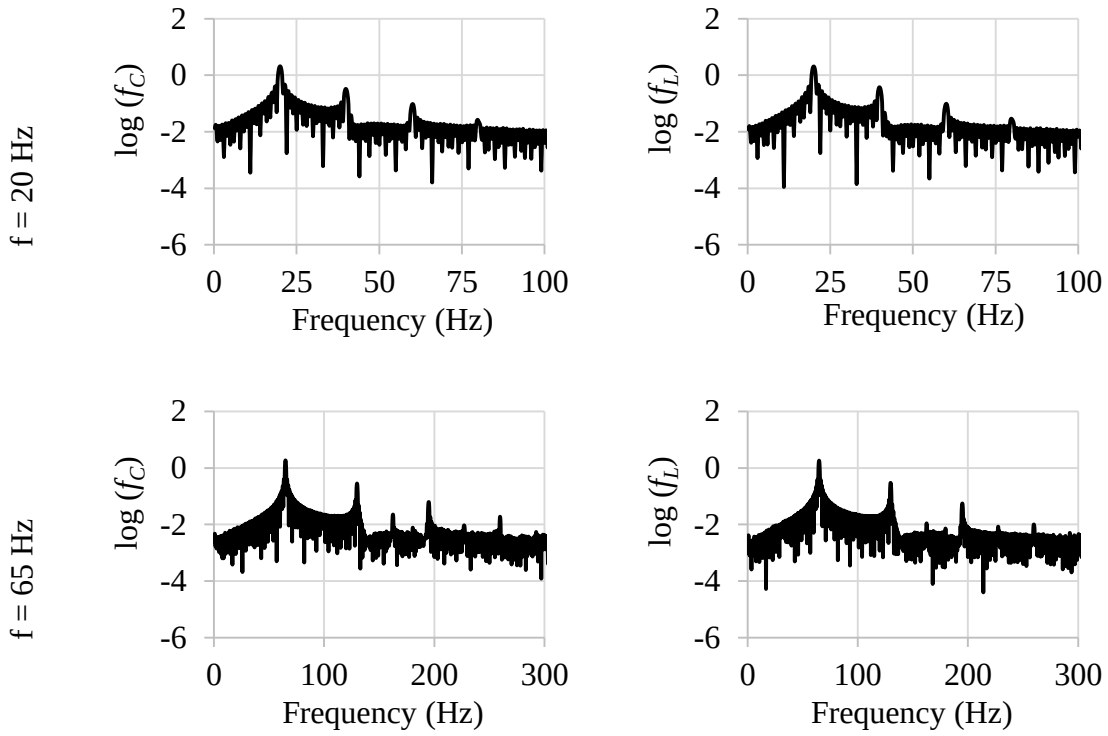

Figure 6– Representative (Sample 4) spectra of the force signal in the *C* (right) and *L* (left) directions obtained at 20 Hz (top) and 65 Hz (bottom).

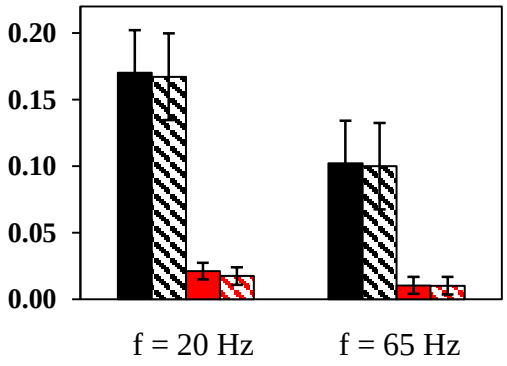

Figure 7– Average values of *THD* (solid fills) and HD_2 (pattern fills) of the force (black) and acceleration (red) signals at 20 and 65 Hz. Error bars represent the standard deviation.

Table 2– Material constants for the aorta samples and R^2 values.

Model Parameters	Sample 1	Sample 2	Sample 3	Sample 4	Sample 5
Viscoelastic parameters					
G_1	0.51	0.49	0.22	0.28	0.24
β_1 (1/s)	71	570	455	301	300
G_∞	0.49	0.51	0.78	0.72	0.76
Instantaneous elastic parameters					
b_{1C} (kPa)	450	125	352	400	145
b_{2C} (kPa)	115	380	10	186	262
b_{3C} (kPa)	4350	7900	5150	5389	1150
b_{4C} (kPa)	650	-2350	-550	5369	-126
b_{5C} (kPa)	-1850	1750	-860	-5455	-301
b_{1L} (kPa)	425	100	310	295	150
b_{2L} (kPa)	50	350	10	5	475
b_{3L} (kPa)	950	-2025	850	1410	750
b_{4L} (kPa)	350	-2150	-100	4080	-1050
b_{5L} (kPa)	-450	3850	160	-2550	150
R^2 – 20 Hz	0.76	0.81	0.95	0.89	0.83
R^2 – 65 Hz	0.95	0.73	0.46	0.85	0.85

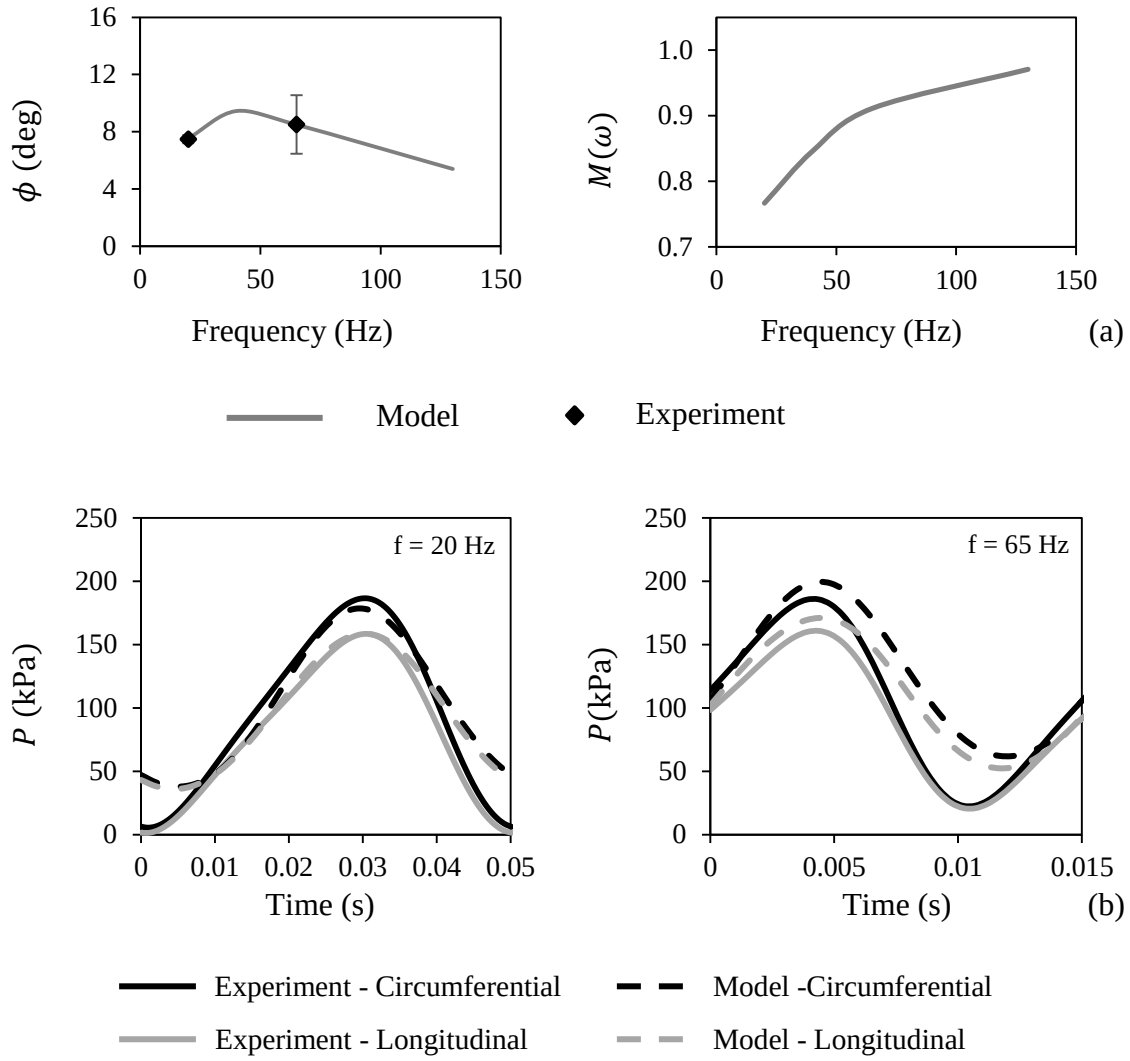

Figure 8– Comparison of model with experiments (Sample 4): a) The reduced complex modulus that fit the phase shift exactly, and b) The oscillating biaxial response for one cycle at 20 and 65 Hz. Overall $R^2 = 0.83$.

Discussion

The rate dependent material properties of human thoracic aorta were characterized in loading rates and deformations that are relevant to TAR. The strain rates reached to about 150 s^{-1} that is higher than previous dynamic studies by Mohan and Melvin (1983) (80 s^{-1}) and Shah et al. (2006) (136 s^{-1}). The oscillatory loading method that was used in this study enabled us to determine the phase shifts between the stresses and strains directly. Based on these phase shifts, the viscoelastic decay rates were found in the range of 70 to 550 s^{-1}. This range is 10 to 100 folds higher that previous viscoelastic models for aorta (Hemmasizadeh et al., 2012). The reduced relaxation functions that were obtained show significant rate dependence before 10 ms (Figure 9), which is critically important in computational modeling of TAR as the rupture occurs typically within 20 ms (Bass et al., 2001). The relaxation decay rates that were estimated based on comparing the dynamic and quasistatic tests of Mohan and Melvin (1983) were also in the range of 400 s^{-1} which agree with the results of this study. One important observation based on the decay rates found in this study is that despite the large variability that is typically seen in the material properties of biological tissues, the decays rates are more or less consistent, which shows that the mechanism of rate dependency at high loading rates is universal and independent of age. This effect is generally attributed to the movement of tissue fibers (elastin and collagen) within the surrounding water molecules (Ghodsi and Darvish, 2015). For the steady state relaxation amplitude (G_∞), two distinct ranges of 0.5 and 0.7 were found which could be attributed to atherosclerosis and arteriosclerosis that are typically happening in human arteries with age (Wang and Bennett, 2012) and may have caused the rise of G_∞ in some samples. However, more samples need to be tested in conjunction with histological studies

to investigate this effect further. In the experiments, one sinusoidal input was used in each direction which was sufficient for characterization of a QLV model but not for a fully nonlinear model with multiple hereditary integral (Darvish, 2009). For this purpose, summation of multiple sinusoidal with different frequencies needs to be applied in each direction, which was beyond the scope of this work.

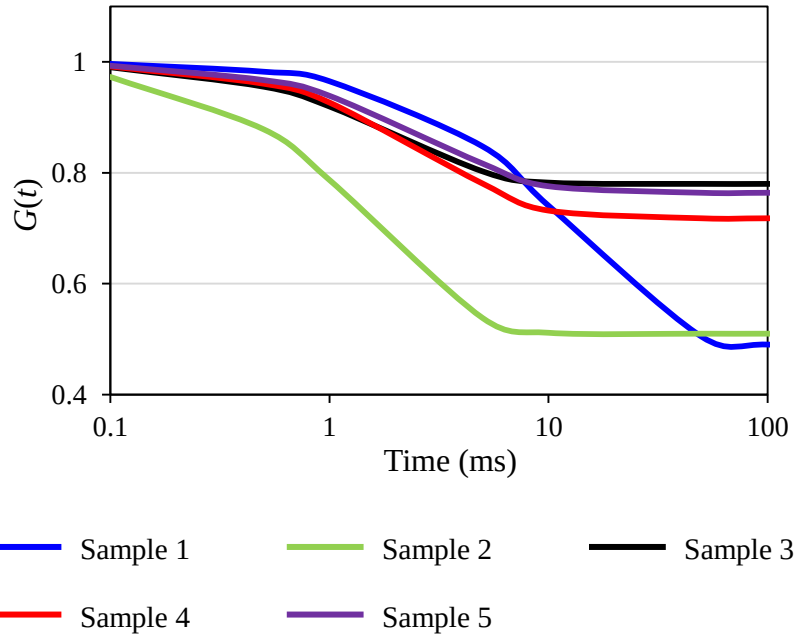

Figure 9– Normalized relaxation function predicted by the model

The phase shifts that were found between stress and strain time histories were different in the *C* and *L* directions, which is an indication of anisotropy in the viscoelastic response of aorta. This anisotropy was ignored in the constitutive Equation (2.8) and for simplicity, the average phase shift values were employed. The results showed that the phase shift in *C* direction was generally higher with the average and standard deviation of the ratio between the phase shifts being 1.42 (0.38). This means that the *C* direction was more

viscoelastic than the *L* direction, which could have important effects in the prediction of TAR as the rupture is believed to occur due to a sudden axial stretch of aorta in combination with circumferential stretch due to high pressures (Richens et al., 2002). A comprehensive characterization of the anisotropic viscoelasticity of aorta would require many more tests and was beyond the scope of this study.

Based on the method of oscillatory biaxial tests, the degree of nonlinearity for the nonlinear elastic behavior of aorta was obtained directly from the experiments and not from curve fitting. This was accomplished by comparing the harmonic distortions of different degrees with the total harmonic distortion of the stress signals (Darvish and Crandall, 2001). The second-order nonlinearity that was obtained was implemented in an explicit biaxial relationship between the stress and strain (Equation 2.9) together with the assumption of positive definiteness of the local stiffness matrix (Equation 2.13). This relationship can be easily implemented in finite element models of TAR and would not require the definition of a strain energy function. The elastic functions that were obtained in this manner are comparable with biaxial dynamic results of Mohan and Melvin (1983) in equibiaxial (equal *C* and *L* strains) loading (Figure 10). Since the oscillatory test results are steady state and therefore preconditioned (Fung, 1993), it is expected that the stiffness obtained for samples would be generally smaller than the stiffness obtained from failure tests. To give a quantitative comparison, at $\varepsilon = 0.2$, the stress-strain curves provided by Mohan and Melvin (1983) give a local stiffness 757 kPa for a 49 year-old specimen and 13,500 kPa for a 60 year-old specimen. For the same strain level, the average and standard deviation of local stiffness values found in this study were 934 (726) and 521 (262) kPa in

the *C* and *L* directions, respectively, i.e., closer to the lower end of the Mohan and Melvin results.

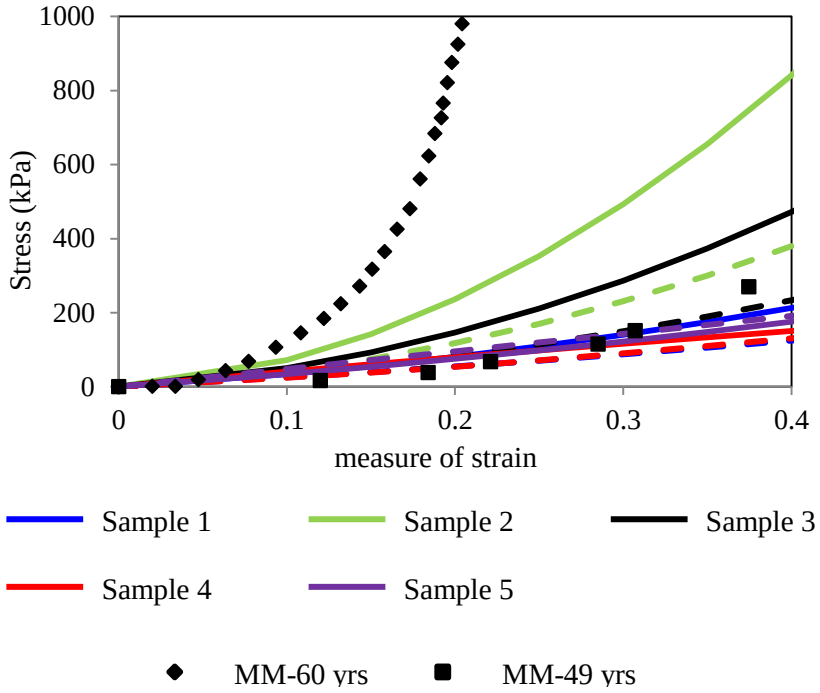

Figure 10– Elastic response predicted by the model for human samples in circumferential (solid lines) and longitudinal (dashed lines) directions. The results of (Mohan and Melvin, 1983, 1982) for 49 and 29 year old aortas are shown for comparison.

The degree of anisotropy in the instantons elastic response of the specimens varied considerably. Some specimen (e.g., Sample 4) were more isotropic and some (e.g., Sample 2) were highly anisotropic. In general, it is believed that aortic tissue becomes structurally and biomechanically more anisotropic with age (Haskett et al., 2010). In this study, we assumed that the principal directions of material anisotropy were the *C* and *L* directions.

While many previous studies have assumed the same (e.g., Rastgar-Agah et al., 2016), some recent studies have the shown that the main directions of the microstructural fibers make an angle with the *C* direction. Hemmasizadeh et al. (2015) showed that only about 5% of elastin and collagen fibers are with ±2.5º of the *C* direction. In a more detailed study, the angle of collagen fibers was reported to be 18.8, 37.8, and 58.9 degrees in the intima, media and adventitia respectively (Schriefl et al., 2012). This angle can be found based on mechanical biaxial tests by measuring the shear strain. However, since the shear strain is generally small, it is difficult to be quantified reliably due to limitation of the resolution in high-speed video images. In a typical anisotropic sample in this study (Sample 1), for maximum strain levels of 0.22 and 0.29 in the *C* and *L* directions, the shear strain was evaluated at 0.07 which corresponds to an angle of about ±58º for the principal axes (Popov, 1990). More samples need to be tested with high-resolution photography in combination with advanced microscopy to determine a relationship between the material anisotropy and the fiber directions.

A main limitation of the oscillatory test method is that the sample and system natural frequencies should be avoided to obtain reliable results for the material constitutive model (Darvish and Crandall, 2001). This limitation is particularly significant as the system natural frequencies start from below 50Hz. For this purpose, only two frequencies could be tested reliably where the harmonics also didn't overlap. Nevertheless, it was shown that sufficient equations could be obtained to characterize the material properties reliably. Another limitation is gripping of the sample with sutures that is time consuming and sometimes damages the sample. The method of gripping with clamps was also tried for

Sample 6 but this method could only work for the lower frequency (20 Hz) and at higher frequencies the clamps cause significant inertial effect and became loose. Our results showed that when clamps were used, the tissue was stiffer. Waldman and Michael Lee (2002) observed a similar trend when applying biaxial quasi-static loading on bovine pericardium samples, using suturing and clamping gripping methods. The samples tested with sutured edges were more compliant compared to the ones with clamped edges. This could also partly explain why the results of Shah et al. (2006) were stiffer than other investigators as they used clamps to attach the samples. They also did not see significant rate dependency which clearly is contradicted by the results of this study. The method of biaxial stretch with sutures is not suitable for failure tests as the material often starts to fail at the suture connections. The forces applied to samples caused deformations beyond the physiological strains (Lillie et al., 2010), up to 10% to 40% strain depending on the sample, but no failure was observed. Therefore, the characterized constitutive model is valid before the tissue failure initiates.

Acknowledgement

The experiments reported here were conducted at the Center for Applied Biomechanics of the University of Virginia. The financial support for the experimental work was provided partly by the National Highway Traffic Safety Administration (NHTSA) under DOT NHTSA Cooperative Agreement DTNH-22-96Y-07029.

CHAPTER 3

INVESTIGATION OF INHOMOGENEOUS MATERIAL BEHAVIOR OF PORCINE THORACIC AORTA USING NANO-INDENTATION TESTS

Introduction

Characterization of the biomechanical behavior of aortic wall is essential for quantifying the effect of diseases on aortic elastic recoil, and also for developing computational models to predict injury and rupture due to pathology or trauma. The focus of previous studies on aorta mechanical behavior has been primarily on the abdominal aorta to address Abdominal Aortic Aneurysm (AAA) (Vorp, 2007) and on thoracic aorta to address Thoracic Aortic Aneurysm (TAA) and Traumatic Aortic Rupture (TAR) (Iliopoulos et al., 2009; Shah et al., 2006). The finite element method has been the main tool in predicting tissue stresses and strains in aorta models (Raghavan et al., 2000; Richens et al., 2004) in most of which, the aortic wall is considered to be a homogeneous and isotropic material. A few studies have shown that the aortic wall is inhomogeneous in the longitudinal (Purslow, 1983; Sokolis et al., 2008; Zeinali-Davarani et al., 2015), circumferential (Choudhury et al., 2009; Kim and Baek, 2011), and radial (Hemmasizadeh et al., 2015; Pena et al., 2015) directions. Also, uniaxial and biaxial tests have shown that the circumferential direction is generally stiffer than the axial direction (Kim et al., 2012; Marra et al., 2006; Mohan and Melvin, 1983, 1982). These studies, however, are not conclusive because they used different methodologies, species, and spatial resolution. The goal of this study was to use a cohesive methodology to characterize the three-dimensional

inhomogeneity as well as anisotropy of thoracic aorta from one set of samples and with high spatial resolution.

The studies that address the inhomogeneity of thoracic aorta mostly used uniaxial and biaxial tests to characterize the mechanical properties. Due to the nonlinear behavior of aorta, the response was divided in either two or three segments based on the range of stress or strain. Regarding the inhomogeneity in the longitudinal direction, there is an agreement that distal sections are stiffer than the proximal ones. This is explained based on the higher ratio of collagen to elastin content in the distal sections determined from X-ray diffraction technique (Roveri et al., 1979) or histology (Sokolis et al., 2008). Additionally, the change in the undulation of collagen fibers in adventitia, with more undulation in the proximal sections, has been associated with this change of stiffness (Zeinali-Davarani et al., 2015). In one of the few studies that address the inhomogeneity in the circumferential direction, the circumference of samples of human ascending thoracic aorta were divided into four small quadrants, which were tested using a biaxial tensile apparatus (Choudhury et al., 2009). This study concluded that the elastic modulus depends on the location of the segment, even though no significant difference was found in the tissue histology. The medial (inner curvature) and lateral (outer curvature) quadrants exhibited the least stiff and the stiffest behavior respectively, in low and high stress states and in both test directions. Kim and Baek (2011) investigated the variations of the biomechanical properties of porcine proximal Descending Thoracic Aorta (DTA) in the circumferential direction using inflation tests and showed that the posterior quadrant was significantly stiffer than the anterior quadrant.

In previous studies conducted in our laboratory, inhomogeneous biomechanical properties of porcine DTA in the radial direction were characterized using a nano-indentation technique and a viscoelastic modeling approach (Hemmasizadeh et al., 2015, 2012). Two distinct layers of equal thickness were determined at the medial quadrant with significantly different material and morphological properties, with an increasing trend in the instantaneous elastic modulus (stiffness), elastic lamella density, total protein, and elastin circumferential percentage from the inner to the outer layers. Pena et al., (2015) studied the layer-specific residual deformation and material properties of porcine DTA and their variations with location along the aortic tree using uniaxial and biaxial tests. Their results showed that the intima and adventitia are generally stiffer and more isotropic than the media in the proximal sections.

In this study, the method of nano-indentation was utilized in three orientations to characterize the inhomogeneity and anisotropy of porcine DTA in three dimensions, i.e., longitudinal, circumferential and radial directions. The spatial resolution is significantly improved compared to previous studies and the experimental results are summarized in the form of viscoelastic models.

Materials and Methods

Tissue Preparation and Testing

Seven fresh porcine aorta specimens were obtained from young pigs (about 6 months old) from a local slaughterhouse (Hatfield Quality Meats, Hatfield, PA). Fat and excessive tissues were removed and six transverse sections (rings), 8-10 mm in length,

were excised from the specimens (Figure 11-a). The sections were divided into three groups according to their location along the aortic tree (z-direction) including Upper-DTA (above the 1st intercostal artery), Mid-DTA (between the 1st and the 2nd intercostal arteries), and Lower-DTA (between the 3rd and 4th intercostal arteries (Hemmasizadeh et al., 2012). In order to investigate the effect of circumferential location (θ-direction), four quadrants, i.e., anterior (ANT), posterior (POST), medial (MED), and lateral (LAT) quadrants, were identified as indicated in Figure 11-b. The wall thickness was measured at the four quadrants for the three section groups. The average (and standard deviation) of the wall thickness was 1.55 (0.54) mm.

Using a custom-made nano-indentation test setup that is described in Hemmasizadeh et al. (2012), indentation tests were performed for material characterization. Briefly, samples were moved upward toward the conical indenter (62.5° semi-vertical angle) with a ramp and hold displacement with 60 μm indentation depth, 25 ms ramp time and 20 s hold time (Figure 12). All the tests were conducted within eight hours post-mortem.

In order to characterize the material properties in three dimensions, first, axial indentations were conducted on about 10 points along the thickness (r-direction) at four quadrants (Figure 11-c). Next, 5-6 mm rectangular blocks were cut from each section at the medial and lateral quadrants, which were used for circumferential and radial indentations (Figure 11-d). Circumferential tests were also performed on about 10 points along the thickness that corresponded approximately to the axial indentation points. The radial tests were conducted on the lumen side ($r = 0$) and repeated at two points. The spatial

resolution of indentation was about 100 μm and the first and last points were about 100 μm from the edge to minimize the boundary effects.

Formulation

A Quasi-Linear Viscoelastic (QLV) constitutive equation was used to describe the relationship between the indenter force history, $P(t)$, and the indentation depth, $h(t)$, for a conical indenter with the semi-vertical angle of β. The formulations used were:

$$P(t) = \int_0^t G(t-\tau)\frac{\partial P^e(h)}{\partial h}\frac{\partial h}{\partial \tau}d\tau \tag{3.1}$$

$$P^e = \frac{1}{\alpha}\frac{2E_0 cot(\beta)}{\pi(1-\nu^2)}\,h^2 \tag{3.2}$$

$$G(t) = G_\infty + \sum_{i=1}^{4} G_i exp(-\beta_i t) \tag{3.3}$$

in which $G(t)$ is the reduced relaxation function describing the time dependency of the response and $P^e(h)$ is the instantaneous elastic force function. E_0 is the instantaneous elastic (Young's) modulus, and ν is the Poisson's ratio which was assumed to be 0.49. α is the correction factor introduced in Hemmasizadeh et al. (2012) that accounts for the non-ideal geometry of the indenter, imperfections in contact area, and the nonlinearity of system compliance among other factors. For the indentation depth used in this study (h = 60 μm), $\alpha \approx 3$. G_i are the reduced relaxation amplitudes and β_i are the corresponding decay rates that were assumed to be constants ($\beta_{1..4}$ = 0.1, 1, 10, 100 s^{-1}) and spanned the four orders of magnitude of time that were in the experiments. For simplicity of data presentation and

analysis, the elastic moduli at specific times of relaxation, corresponding to $t = 0, 0.01, 0.1, 1, 10, \infty$ s, were calculated from the elastic relaxation function:

$$E(t) = E_0 G(t) \tag{3.4}$$

The QLV material parameters (Equations 3.2 and 3.3) were determined by comparing the experimental data with the model and a least square optimization for G_i and E using an *in-house* MATLAB code. The relaxation data was resampled logarithmically to give approximately equal weights to different time scales. The moduli measured from indentations conducted in the axial, circumferential, and radial orientations are represented by subscripts A, C, and R, respectively (Figure 11-c and d).

Statistical Analysis

The statistical analysis was performed, using JMP SAS, Version 11, Cary, NC. To determine whether the elastic moduli were significantly dependent on the orientation of indentation (A, C and R), as well as the three-dimensional locations, z (Upper-, Mid-, and Lower-DTA), θ (ANT, LAT, MED, and POST quadrants), and r (11 regions), a 4-factor multi-variate analysis of variance (MANOVA) followed by Tukey's HSD *post-hoc* test was conducted. Additional *post-hoc* contrast analysis was performed to evaluate whether adjacent regions in the radial direction can be grouped in significantly distinct layers. The effect of relaxation was studied as an additional factor with repeated measures. In order to eliminate the inter-specimen variability in comparing the data, all the analyses were paired. The results are presented as mean (standard deviation) and standard error of the mean is used for the error bar in the graphs. The threshold for the *p*-value to indicate statistical significance was considered at 0.05.

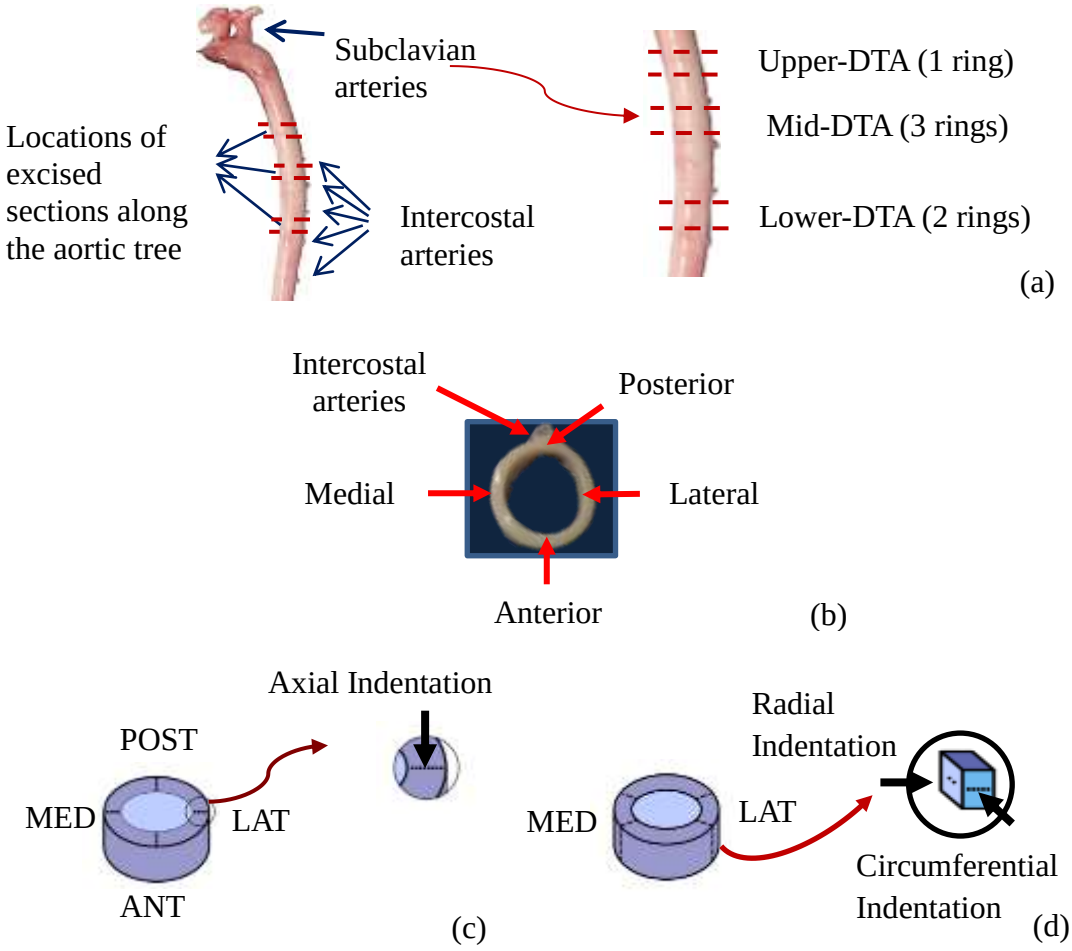

Figure 11– a) Locations of excised sections (rings) along the descending thoracic aorta (DTA). b) Top view of a cylindrical section with the medial, anterior, lateral, and posterior quadrants marked. c) Schematic representation of the locations of axial indentation, d) Schematic diagram of the locations for radial and circumferential indentations on excised blocks at the medial and lateral quadrants.

Results

The samples wall thickness results are summarized in Table 3 which shows that the values generally decreased from proximal to distal sections and were dependent on the quadrant. The thickness in Lower-DTA was significantly smaller than Upper- and Mid-DTA ($p < 0.0001$). The highest and lowest thicknesses were in the ANT and POST quadrants and the two were significantly different ($p = 0.020$).

Table 3– Aortic wall thickness grouped by quadrant and section.

θ – Quadrant	Thickness (mm)	z – Section	Thickness (mm)
ANT	1.72 (0.67)	**Upper-DTA**	1.87 (0.33)
LAT	1.51 (0.51)	**Mid-DTA**	1.82 (0.42)
MED	1.59 (0.45)	**Lower-DTA**	0.99 (0.29)
POST	1.33 (0.60)		

Figure 12 shows representative force and displacement time history curves of a typical indentation test and provides a comparison between the experimental data with the corresponding QLV model. This comparison demonstrates that the viscoelastic model force closely followed the experimental force data. The transient vibration observed in the force data (due to the sample natural frequencies) was relatively small and ignored in the viscoelastic characterization.

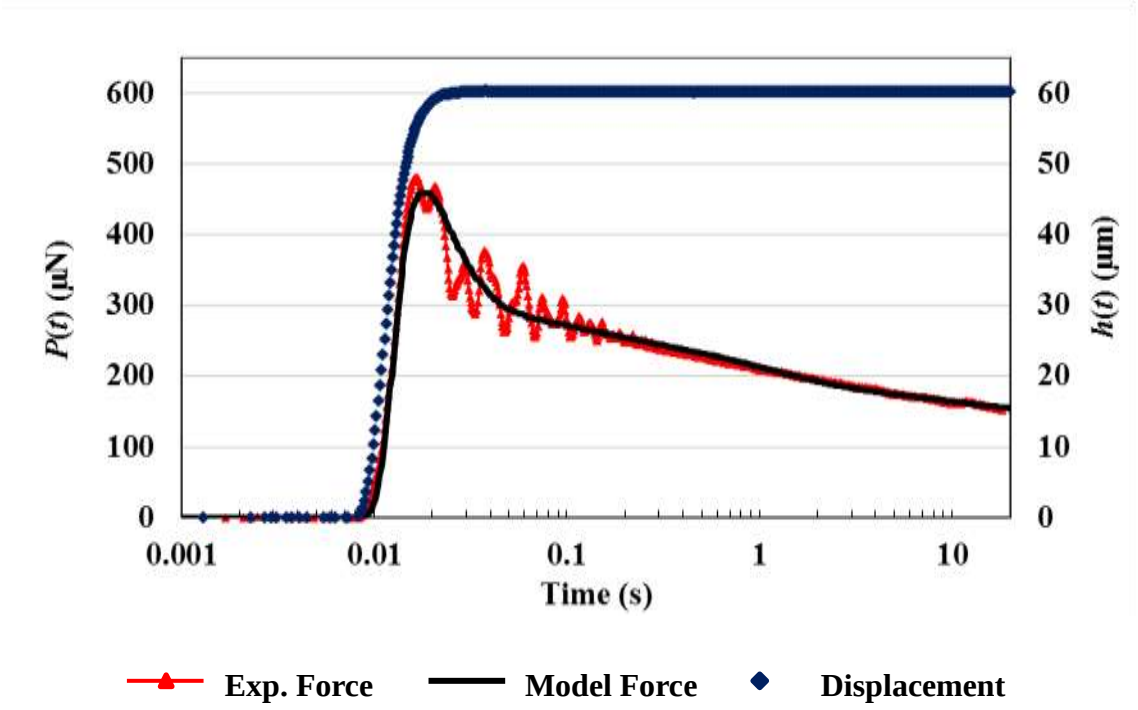

Figure 12– Force and displacement time history curves from a typical indentation test and comparison with the corresponding QLV model.

Tissue Anisotropy

Comparison of $E_C(t)$ and $E_A(t)$, when pooled for z, θ, and r directions, showed that they are significantly different (Figure 13-a) with $E_C(t) > E_A(t)$ ($p < 0.001$). Specifically, on average, the circumferential direction was 13 and 25 % stiffer than the axial direction for $E(0)$ and $E(\infty)$, respectively. The difference between the circumferential and longitudinal moduli changed with z-, θ-, and r-directions. When the effect of z was separated, the anisotropy was significant in Mid- and Lower-DTA ($p < 0.002$) with $E_C(0)/E_A(0) = 1.17$ in both sections; however, anisotropy was not significant in the Upper-DTA ($p = 0.300$) where $E_C(0)/E_A(0) = 1.02$. When the effect of θ was separated,

the anisotropy was significant at LAT quadrant (p < 0.00002) but was not at MED quadrant (p = 0.167). Quantitatively, $E_C(0)$ was 25% stiffer than $E_A(0)$ at LAT quadrant compared with 3% at MED. These effects are demonstrated for E_0 in Figure 13-b and c. At the lumen side (r = 0), the elastic relaxation function in three directions were compared (Figure 13-d) and it was found that $E_C(t)$ and $E_R(t)$ were indistinguishable (p = 0.461) and $E_A(t)$ was significantly lower (p < 0.0002). The effect of r-direction on the anisotropy was more pronounced in Layer I (p < 0.001) with $E_C(0)/E_A(0) = 1.29$.

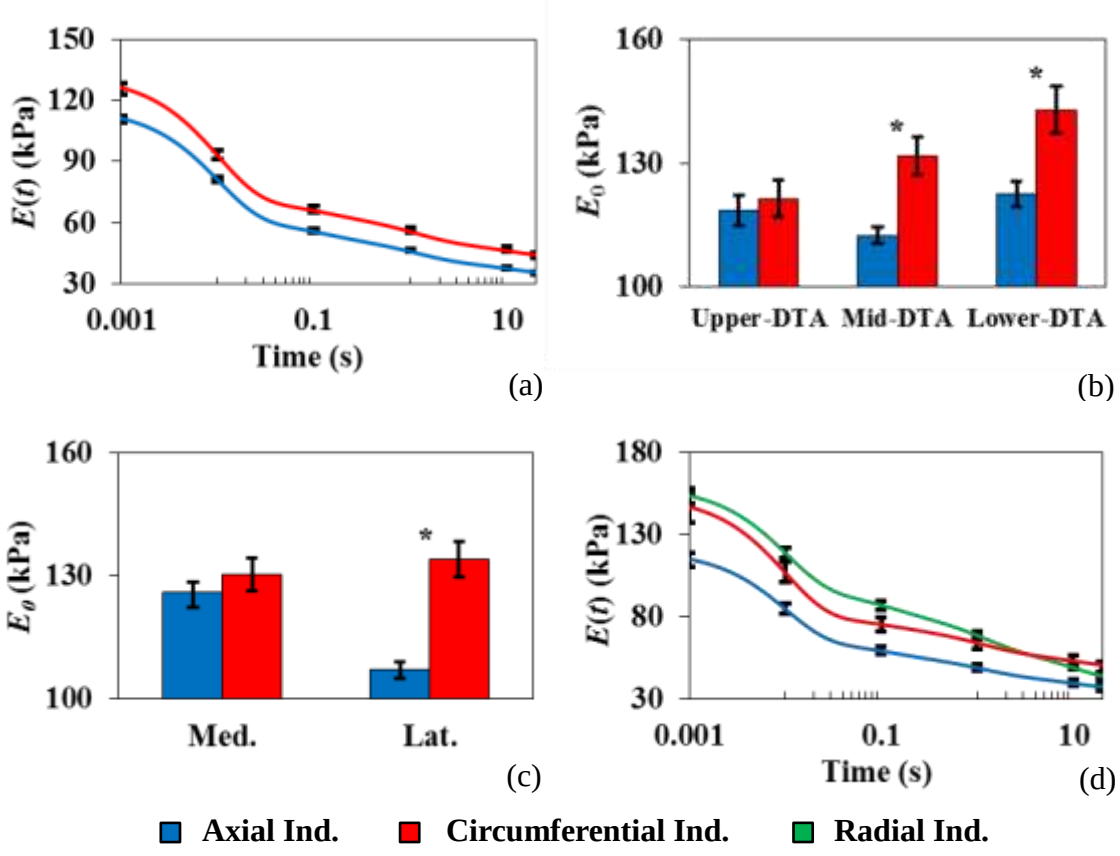

Figure 13– Elastic relaxation function obtained from indentation tests at different orientations when pooled data for medial and lateral quadrants a) along the aortic thickness and d) at r = 0; Variation of $E(0) = E_0$ with b) z-direction and c) θ-direction

Tissue Inhomogeneity

To quantify the tissue inhomogeneity, the changes in $E_A(t)$, $E_C(t)$, and $E_R(t)$ based on the three-dimensional location were studied separately. The pooled values for each dimension are summarized in Table 4 and are explained below. To determine the values in each row of this table, the other two dimensions were averaged. More detailed tables of data with additional sub-groups are provided as supplementary material.

Effect of r-direction

The position along the *r*-direction (thickness) was normalized, where r = 0 and 1 represented the innermost and outermost layers, respectively and categorized into 11 regions as r_0 = 0..0.05, r_1 = 0.05..0.15, …, and r_{10} = 0.95..1.0. In order to clarify how $E_A(t)$ and $E_C(t)$ depend on *r*, the elastic relaxation functions were normalized based on the average E_A for each specimen. This normalization eliminated the inter-specimen variability and showed that 4 layers could be distinguished. The innermost layer (Layer I: r_0-r_1), with a relatively high stiffness, included the elastic lamina interna (Mills, 2007). The next two layers (Layer II: r_2-r_5 and Layer III: r_6-r_9), were named inner and outer media and had relatively low and high stiffness respectively. The last layer (Layer IV: r_{10}), corresponded to the adventitia and showed the lowest stiffness. The variations of the normalized $E_A(t)$ and $E_C(t)$ at t = 0, designated by $\bar{E}_A(0)$ and $\bar{E}_C(0)$, are depicted in Figure 14 overlaid on a representative section of porcine aorta. The aorta section was stained with a Verhoeff-van Gieson protocol that showed elastin fibers as dark brown and collagen fibers as light red. The contrast analysis results showed that Layer I was stiffer than Layer II (p = 0.034 for $E_A(t)$, p = 0.005 for $E_C(t)$), and Layer III was also stiffer than Layer II, while this result

was not significant for $E_C(t)$ (p = 0.019 for $E_A(t)$, p = 0.140 for $E_C(t)$). Layer IV was significantly more compliant than all other Layers (p < 0.0001).

Effect of z-direction

There was generally an increase in the elastic moduli from proximal to distal aortic sections in all three indentation orientations (Table 4). In terms of $E_A(t)$, Upper-DTA was not statistically different from Mid- and Lower-DTA (p = 0.069 and 0.058, respectively); however Mid-DTA was statistically less stiff than Lower-DTA (p = 0.0006). In the case of $E_C(t)$, Mid-DTA was not statistically different from Upper- and Lower-DTA (p = 0.242 and 0.067, respectively) while Upper-DTA was statistically less stiff than Lower-DTA (p = 0.002). In the radial indentation results, the increases in $E_R(t)$ versus z were all statistically significant (Upper- vs Mid-DTA: p = 0.035; Upper- vs Lower-DTA: p <0.0001; Mid- vs Lower-DTA: p = 0.012). Comparison of the instantaneous elastic moduli showed that the lower-DTA was 12%, 18%, and 26% stiffer than the Upper-DTA in axial, circumferential, and radial indentation, respectively (Table 4).

Effect of θ-direction

The axial indentation results (Table 4) showed that $E_A(t)$ was significantly more compliant in the MED quadrant (p < 0.005). However, a more detailed analysis showed that this effect was only significant in the Mid- and Lower-DTA (p<0.007) but not in Upper-DTA (p = 0.117). For the other two orientations, comparison between LAT and MED quadrants showed that they are statistically indistinguishable (p = 0.453 for $E_C(t)$ and p = 0.381 for $E_R(t)$). More detailed analysis showed that for $E_C(t)$, the MED quadrant

in Upper-DTA was, in fact, significantly stiffer than LAT (p = 0.0003), e.g., for $E_C(0)$ the MED is 23% stiffer than LAT.

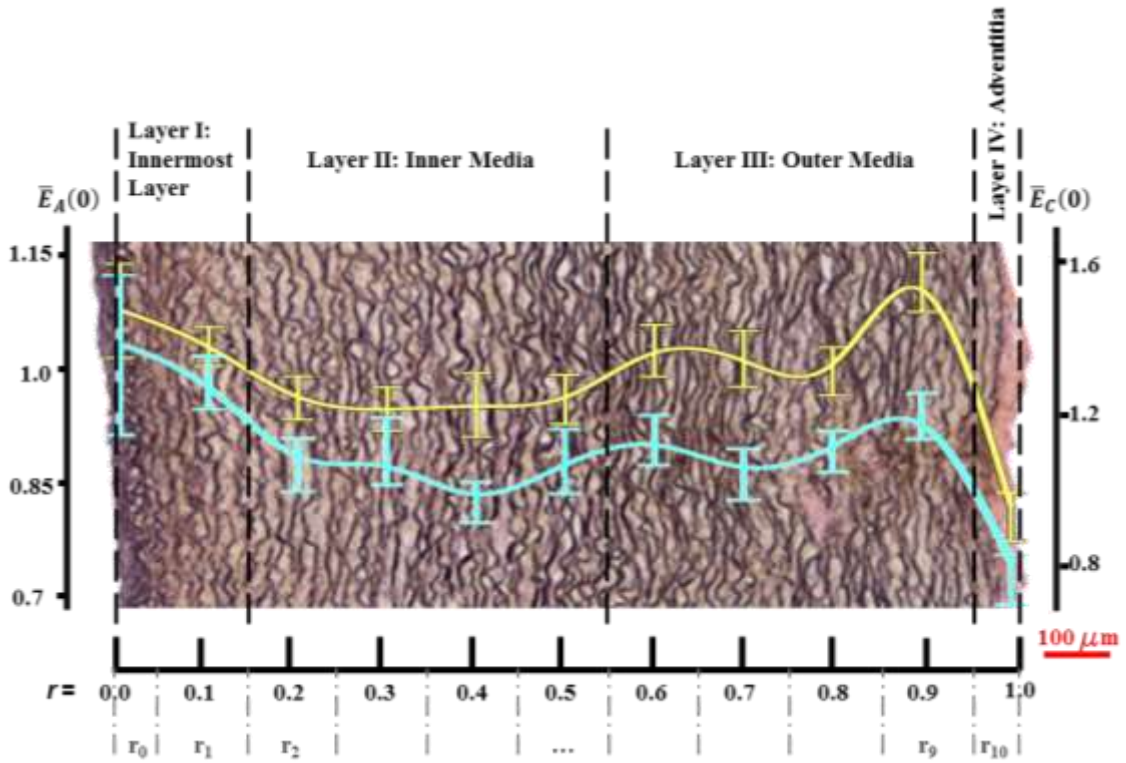

Figure 14– Variation of average normalized elastic moduli along the thickness of the aorta overlaid on a representative section of porcine DTA. The innermost layer (Layer I: r_0-r_1), with a relatively high stiffness, included the elastic lamina interna. The next two layers (Layer II: r_2-r_5 and Layer III: r_6-r_9), were named inner and outer media and had relatively low and high stiffness respectively. The last layer (Layer IV: r_{10}), corresponded to the adventitia and showed the lowest stiffness. Axial (left axis) and circumferential (right axis) indentation results are shown in yellow and cyan, respectively. Verhoeff-van Gieson protocol is used which shows elastin fibers as dark brown and collagen fibers as light red.

Table 4– Elastic moduli at different relaxation times grouped by section, quadrant, and layer for a) Axial, b) Circumferential, and C) Radial indentations

	E_0 (kPa)	$E(0.01)$ (kPa)	$E(0.1)$ (kPa)	$E(1)$ (kPa)	$E(10)$ (kPa)	$E(\infty)$ (kPa)
a) Axial Indentation						
***r* – Layer**						
Layer I	123.73 (37.15)	86.94 (26.43)	60.67 (19.55)	50.22 (16.97)	40.80 (14.63)	37.53 (13.91)
Layer II	114.10 (37.51)	79.38 (26.83)	54.30 (19.55)	44.57 (16.58)	36.46 (13.9)	33.78 (13.03)
Layer III	123.99 (42.51)	86.17 (29.93)	59.42 (21.47)	49.28 (18.17)	40.44 (15.11)	37.49 (14.09)
Layer IV	94.76 (27.68)	64.98 (20.08)	44.02 (15.08)	36.02 (13.36)	29.29 (11.59)	27.20 (10.95)
***z* – Section**						
Upper-DTA	118.44 (34.25)	83.38 (25.84)	58.49 (20.22)	49.03 (18.02)	40.58 (16.15)	37.65 (15.64)
Mid-DTA	112.11 (36.46)	77.87 (25.70)	53.37 (18.56)	44.03 (15.81)	36.20 (13.18)	33.64 (12.28)
Lower-DTA	132.49 (44.48)	92.25 (31.43)	63.58 (22.56)	52.31 (19.05)	42.28 (15.96)	38.88 (14.96)
***θ* – Quadrant**						
ANT	123.26 (40.35)	85.66 (27.96)	59.03 (19.67)	48.77 (16.54)	39.82 (13.68)	36.86 (12.73)
LAT	126.04 (39.88)	88.07 (28.50)	60.89 (20.85)	50.40 (17.84)	41.43 (15.08)	38.45 (14.16)
MED	107.22 (29.87)	74.76 (21.86)	51.52 (16.67)	42.56 (14.61)	34.78 (12.62)	32.14 (11.99)
POST	125.46 (51.64)	86.58 (36.30)	58.93 (25.78)	48.34 (21.54)	39.27 (17.49)	36.30 (16.07)
b) Circumferential Indentation						
***r* – Layer**						
Layer I	154.00 (56.6)	106.85 (39.45)	75.28 (28.64)	64.22 (25.19)	53.09 (21.25)	49.20 (19.90)
Layer II	125.49 (46.74)	88.41 (34.70)	62.68 (26.84)	53.04 (23.82)	44.28 (20.73)	41.35 (19.64)
Layer III	132.48 (43.42)	94.57 (31.73)	68.03 (23.99)	57.63 (21.13)	48.27 (18.22)	45.21 (17.26)
Layer IV	100.32 (29.13)	70.51 (21.17)	49.74 (16.40)	41.28 (14.79)	33.18 (13.32)	30.42 (12.93)
***z* – Section**						
Upper-DTA	121.32 (41.66)	86.09 (30.65)	61.36 (23.37)	51.66 (20.78)	42.67 (17.99)	39.57 (17.07)
Mid-DTA	131.77 (43.86)	92.39 (31.35)	65.33 (23.23)	55.26 (20.18)	45.98 (17.21)	42.93 (16.22)
Lower-DTA	142.98 (54.27)	101.39 (39.33)	72.77 (29.81)	62.09 (26.47)	52.25 (22.74)	48.99 (21.40)
***θ* – Quadrant**						
LAT	130.42 (45.39)	92.24 (32.72)	65.84 (24.65)	55.74 (21.77)	46.49 (18.76)	43.45 (17.71)
MED	134.05 (49.91)	94.63 (36.27)	67.35 (27.4)	57.13 (24.24)	47.62 (20.88)	44.40 (19.76)
c) Radial Indentation (lumen side)						
***z* – Section**						
Upper-DTA	141.41 (36.74)	105.35 (27.64)	77.15 (21.3)	60.92 (18.23)	43.56 (14.66)	36.55 (13.17)
Mid-DTA	159.47 (39.07)	118.44 (26.89)	86.16 (18.9)	67.20 (16.31)	47.63 (13.73)	39.98 (12.81)
Lower-DTA	177.88 (42.05)	131.71 (30.14)	96.63 (22.68)	77.68 (20.48)	56.57 (17.38)	47.82 (15.97)
***θ* – Quadrant**						
LAT	163.68 (45.18)	120.89 (31.9)	87.86 (23.53)	69.37 (20.75)	49.98 (17.29)	42.32 (15.82)
MED	155.50 (37.92)	116.11 (28.02)	85.43 (21.12)	67.82 (18.28)	48.52 (15.01)	40.58 (13.56)

Discussion

The material behavior of porcine DTA was characterized using a nano-indentation technique and QLV modeling. Using this method, the inhomogeneity or spatial resolution of the material properties, compared with existing data that are primarily obtained from uniaxial and biaxial tests (e.g., Sokolis et al., 2008; Zeinali-Davarani et al., 2015) was substantially improved. Particularly, the material properties were characterized across the aorta thickness in 10 locations that to the best of our knowledge has not been done before. The spatial resolution was approximately 100 μm since the test area was a circle with 62 μm diameter and the distance between two test sites was 100 μm.

In order to quantify the tissue local anisotropy, the indentation tests were conducted in two (or three at $r = 0$) perpendicular orientations on the same sample. The material elastic moduli that were obtained using Equation (3.2), i.e., E_A, E_C, and E_R, are based on the equivalent isotropic solution, which is shown to be valid for axisymmetric indenters and an anisotropic half-space (Vlassak et al., 2003). They are not, however, equivalent to the cylindrical anisotropic moduli in the longitudinal (E_z), circumferential (E_θ), and radial (E_r) directions. The tissue in the vicinity of the indenter undergoes a complex state of stress (Fischer-Cripps, 2007). However, since the compressive stress in the direction of indentation is the dominant component, it is expected that E_A would be more affected by E_z, E_C by E_θ, and E_R by E_r.

The mean stress experienced by the tissue under indentation loading in this study is approximately 60 to 90 kPa. The corresponding obtained E_A (0) is consistent with the range of 80-170 kPa reported by Sokolis et al. (2008) for axial elastic modulus of porcine

DTA in the physiologic stress region (40-80 kPa). The results of the current study for $E_A(0)$ are on average 64% stiffer than the values reported by Hemmasizadeh et al. (2012) which can be explained by the tissue nonlinearity with respect to the depth of indentation. The indentation depth in the current study (60 μm) was 50% higher than theirs (40 μm).

The majority of previous studies have also reported that human and porcine DTA exhibit higher stiffness in the circumferential direction compared to the axial direction although the ratios vary considerably (e.g., Peña et al., 2015; Purslow, 1983; Shah et al., 2006). The effect of anisotropy was more pronounced in the distal sections which is in agreement with the results of Zeinali-Davarani et al. (2015) where a similar trend was observed. The degree of anisotropy was more pronounced in Layer I which is consistent with the trend observed by Pena et al. (2015) where the intima was more anisotropic than the media as going from proximal to distal sections.

There was an increasing trend observed in E from proximal to distal sections which is consistent with previous studies (Pena et al., 2015; Purslow, 1983; Sokolis et al., 2008; Zeinali-Davarani et al., 2015) where this change was associated primarily with the collagen content and their undulation. Zeinali-Davarani et al. (2015) found that in distal sections compared with proximal ones, the collagen fibers had a larger contribution to the mechanical properties compared to elastin and an earlier engagement in the load bearing process.

The fact that the medial quadrant was significantly more compliant than the other quadrants in axial indentations is in agreement the results of Choudhury et al. (2009) for human ascending aortic tissue (58 ± 11 yrs).

The aorta wall thickness was divided into more sub-layers compared to Hemmasizadeh et al. (2012), which was focused only the axial indentation at the medial side. In order to compare the findings of the current study with their results, the average values of $E_A(0)$ at the medial quadrant were found in the inner half (r_1 - r_5) and the outer half (r_6 - r_9). The outer half found to be 12% stiffer than the inner layer (113.66 (32.27) vs 101.58 (26.69) kPa), which was similar to what they found (15% increase). This increase in the stiffness of the media from the inner layers toward the outer ones has been shown to be strongly related to certain wall morphological quantities, i.e., the elastic lamellae density, the total protein content and the elastin circumferential percentage of fibers (Hemmasizadeh et al., 2015).

In our results for across the thickness, two radial locations, r_0 and r_9, showed relatively higher stiffness, which can be associated with the elastic lamina interna and externa, respectively (Oie et al., 2009). In the last radial location, r_{10}, that encompasses the adventitia, the stiffness was decreased significantly. Zeinali-Davarani et al. (2015) showed that the collagen fibers in media, regardless of their location along the aorta, are recruited gradually from the beginning of loading, while in adventitia, they start to become load bearing with a delay. This delay can partly explain why in nano-indentation tests, where the deformations are small, the adventitia would yield a lower stiffness. The results reported by Pena (2015), however, show that the adventitial was generally stiffer than the media. It should be noted that the outer layer in their study was 0.67 ± 0.15 and 0.55 ± 0.03 mm for proximal and distal DTA, respectively, and therefore thicker than layer r_{10}, which

suggests that some of the media, especially the elastic lamina externa may have been included in their outer layer.

The distributions of stresses in aorta can be highly affected by the residual stresses present in the tissue (Han and Fung, 1996). In the test method used here, the axial residual stress was clearly released but in the axial indentation tests, the circumferential residual stress was preserved. In case of circumferential and radial indentations, the circumferential residual stress was also released to expose the surfaces. It is therefore possible that the anisotropic ratio between E_C and E_A was underestimated.

Aging can significantly affect the aortic tissue anatomy and material properties. It has been shown that after age 60, the human aorta becomes stiffer and more anisotropic due to the changes in the tissue microstructure (Haskett et al., 2010). In this study, porcine aorta was used as a surrogate for young and healthy human aorta. For this reason, the sections of DTA contained mostly media and showed no arterial wall disease. The methodology presented here needs to be applied to human DTA tissue in the future to characterize the effects of aging, diseases such as atherosclerosis, and changes in the microstructural anatomy.

The results of this study deal with the material behavior of aorta in the initial linear (toe) region of its generally nonlinear mechanical response. However, it is expected that the trends that were observed in the linear region would continue in the nonlinear region although, perhaps, with different ratios. For example, our results showed that the medial quadrant in axial indentation was more compliant compared to the other quadrants. As the failure in aorta is primarily strain based (Mohan and Melvin, 1983), this result would

predict that in axial loading, DTA failure should start from the medial side. This prediction agrees with the clinical observations in patients who experienced TAR (medial and inner: Bertrand et al., (2008)) and the experimental work that show axial loading of aorta as one of the primary mechanisms of rupture (Shah et al., 2006).

CHAPTER 4

EFFECT OF INHOMOGENEITY AND RATE DEPENDENCY OF AORTA ON THE PREDICTION OF INJURY USING GHBMC FBM

Introduction

Traumatic Aortic Rupture (TAR) is the second most common cause of fatal injuries observed in automotive accidents only after traumatic brain injury with survival rates of less than 10% in the field and less than 2% overall (Plummer et al., 2006; Richens, 2003). Consequently mitigation and prevention of TAR is of paramount importance. Safety devices, such as airbags and seat belts, are used extensively compared to the past decades; nevertheless high risks of TAR are still present in car crashes, particularly, the risk of TAR in frontal crashes has increased compared to the past (e.g. Ryb et al., 2013). Hence, it is essential to develop better models for injury/failure prediction for improving the injury prevention systems in frontal car crashes.

More than 90% of aortic ruptures occur with a transverse intimal tear at the peri-isthmus region, which is a transition region between a relatively mobile heart and a relatively fixed descending thoracic aorta (DTA). Other sites of rupture include ascending thoracic aorta (ATA) and distal DTA (Viano, 1983). Despite the fact that TAR is a significant public health problem, there is still uncertainty regarding the mechanisms of this injury. Various hypotheses have been proposed including axial stretching, intravascular pressure, osseous pinch, and water hammer effect (Richens et al., 2002). Since experimental reproductions of such complex loadings and deformations in cadaveric

surrogate tests have been inconclusive (Cavanaugh et al., 2005), finite element (FE) modeling is the preferred method to gain better insights into the mechanisms of TAR as a result of blunt chest trauma.

Few FE studies have focused on simulating the aortic response to various loading modes representative of car crashes (Belwadi et al., 2012; Richens et al., 2004; Shah et al., 2001). One of the first detailed FE models of human chest was developed by Shah et al., (2001) in order to simulate seven impact tests centered at the level of the thoracic vertebra T8 at 30-degree intervals. The peri-isthmus region experienced the highest principal stresses in all impact scenarios. Their results showed that aorta is more prone to rupture at lateral right-sided impacts than any other impact direction. In frontal impacts, the isthmus, the ATA and mid-DTA were most likely to rupture. Richens et al., (2004) developed a thorax model and extracted the motion response of the heart following a simulated thoracic frontal impact and applied it in a second more detailed FE model of the heart and aorta. The results showed that the maximum stresses occur at the isthmus and pulmonary artery bifurcation. Belwadi et al., (2012) reconstructed eight near side left lateral impacts, where TAR occurred, using the Crash Injury Research and Engineering Network (CIREN) database, FE models of the vehicles, and the Wayne State Human Body Model–II (WSHBM). Their model prediction of high strain regions in the aorta matched the data observed at the autopsy where the peak maximum principal strains occurred in the peri-isthmus region.

With advancements in medical imaging techniques in the past decades, detailed anatomical geometry of the human body are available for FE simulations. However, there

are some shortcomings associated with the existing models in regards to the soft tissue material properties, fluid/solid interaction (FSI), and contacts between the organs. In terms of materials properties, most existing models are simplistic and not representative of aortic characteristics, e.g., nonlinearity, anisotropy, and rate dependence. However, our studies, as well as results from other groups show that thoracic aorta is inhomogeneous (Choudhury et al., 2009; Hemmasizadeh et al., 2015; Sokolis et al., 2008), anisotropic, nonlinear, and viscoelastic (e.g., Mohan and Melvin, 1983; Shah et al., 2006).

The objective of this study was to test the hypothesis that the inhomogeneity and rate dependency of thoracic aorta (TA) has a significant effect on the assessment of injury. For this purpose, aortic material properties were varied within an expected range in one of the most advanced existing FE models of a mid-sized male and the changes in the stress and strain distributions due to a simulated frontal chest impact were compared. The results will be specifically useful in better elucidating the mechanisms of TAR, improving car safety and injury prevention systems, and clinical treatment of the injury.

Methods

The commercially available FE model, Global Human Body Models Consortium (GHBMC, MI) of Full Body Model (FBM) of the 50th percentile male (M50, V4.1) was used in this study in order to investigate the effect of biomechanical properties of aortic tissue on the risk of aortic injury (GHBMC). GHBMC is a consortium of seven automakers and one supplier to consolidate their individual research and development activities in human body modeling into a single global effort to advance crash safety technology. All simulations were run using LS-DYNA (R. 4.2.0; LSTC, Livermore, CA) and each

simulation required approximately 22 hours to complete 50 ms of simulation time using our Dell T7500 workstation with two quad Xenon processors and 24 GB of RAM.

In the original model, the aorta is modeled with shell elements with linear elastic material and filled with elastic solid fluid, i.e., the tissue inhomogeneity, anisotropy, and rate dependency are ignored. There is a broad range of material properties for human aortic tissue in the literature depending on many factors such as the experimental test methods, applied strain rates, and sample location. In order to minimize the changes made in the original model, the aorta model in the FBM was considered as the basis for implementing the inhomogeneous and viscoelastic models. Table 5 lists the element types and material models of the aorta, blood, and human heart in the original GHBMC FBM. We refer to this as the homogeneous model or HM.

Table 5– Material characteristics of the thorax model in original GHBMC (HM)

Tissue	Element Type	Material Model (ID)	Material Coefficients
Aorta	Shell	Linear elastic (1)*	$\rho = 1.0\ g/cm^3,\ E = 8.87\ MPa,\ v = 0.4$
Blood	Solid	Elastic fluid (1)	$C = 1.085\ kPa$, $B_1 = 24.26$, $B_2 = 40.52$, $B_3 = 1.63$, $P = 2.4825\ GPa$
Heart	Solid	Hyperelastic (128) **	$\rho = 1.0\ g/cm^3,\ K = 2.2\ MPa,\ v = 0.45$

* Yuen, (2009)
** Deng et al., (1999)

Inhomogeneity

As in HM, for the inhomogeneous models, the aorta was modeled using the linear elastic material formulation (MAT_001) and only the modulus of elasticity *E* was changed. In order to make an inhomogeneous model along the aortic tree (IHM_L), TA was divided

into 5 sections including ATA, Aortic Arch, Upper-DTA, Mid-DTA, and Lower-DTA (Figure 15-a). The region just distal to the left subclavian artery, i.e., a set of elements in Aortic Arch that were next to Upper-DTA, was designated as Isthmus. The Lower-DTA generally shows the stiffest response; therefore *E* for this section was chosen to be the same as in HM. Based on *in-house* experiments, reported in the previous chapters, and Sokolis et al. (2008), the ratios of *E* values between various sections with respect to Lower-DTA were calculated and the corresponding values were assigned to the aorta (Table 6 first column).

In order to implement the inhomogeneity in the circumferential direction as well as the longitudinal direction (IHM_{LC}), the circumference of IHM_L at each section, was further divided into 4 quadrants, i.e., anterior, lateral, medial, and posterior (Figure 15-b). *E* was calculated for each quadrant based on *in-house* nano-indentation experiments and Choudhury et al. (2009) biaxial tensile tests. The average of value for Lower-DTA was set equal to IHM_L and the other ratios were calculated accordingly (Table 6 columns 2 to 5).

Rate Dependency

The rate dependent behavior of the aorta was modeled by assigning a linear viscoelastic material formulation (MAT_006) to HM. In this material, the shear relaxation behavior is described by:

$$\mu(t) = \mu_\infty + (\mu_0 - \mu_\infty)e^{-\beta t} \tag{4.1}$$

in which μ_0 and μ_∞ are the short- and long-term shear moduli and β is the decay constant. μ_∞ was assumed to be the same as HM (3.17 MPa). Based on previous viscoelastic models of aorta (Hemmasizadeh et al., 2012), the ratio μ_∞/μ_0 was considered to be 0.34 and as a

result μ_0 was set to 9.32 MPa. Based on the results of Chapter 2, it is expected that the values for β that are relevant to TAR to be between 50 and 200 s^{-1} or 0.05 and 0.2 ms^{-1}. Therefore, to investigate the effect rate dependency, the FBM with a model viscoelastic aorta model with $\beta = 0.2$ ms^{-1} (VE0.20) was compared with the one with $\beta = 0.05$ ms^{-1} (VE0.05).

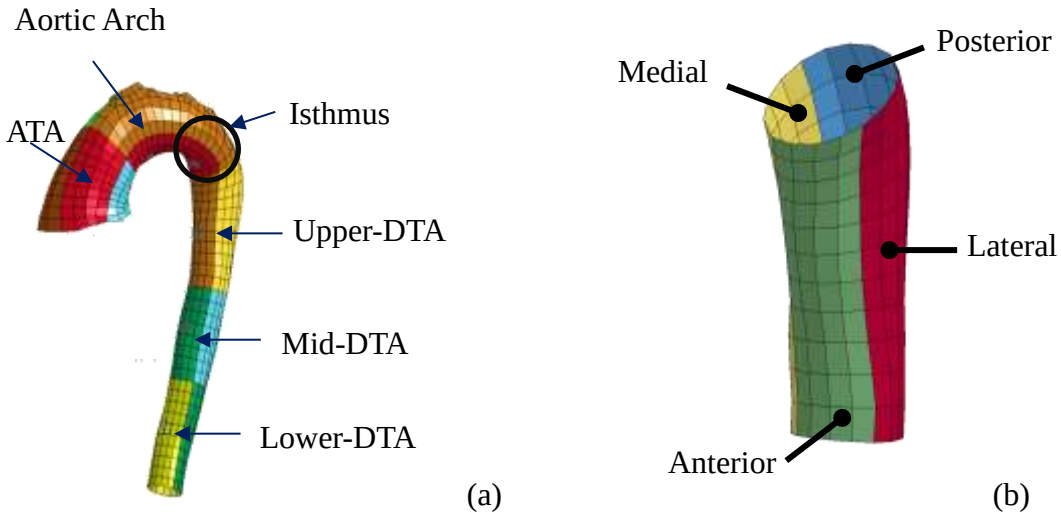

Figure 15– A view of the thoracic aorta showing a) different sections along the aortic tree in IHM_L and b) different quadrants on the aortic circumference in IHM_{LC}.

Table 6– Aorta elastic modulus, E (MPa), in IHM_L and IHM_{LC}

	IHM_L	**IHM_{LC}**			
Section	***E* (MPa)**	**Anterior**	**Lateral**	**Medial**	**Posterior**
ATA	5.79	5.26	7.28	3.49	7.14
Arch	6.03	6.26	7.63	7.92	7.26
Upper-DTA	7.85	6.26	7.63	7.92	7.26
Mid-DTA	7.56	7.27	8.02	6.75	7.38
Lower-DTA	8.87	9.93	9.04	7.05	10.24

Blunt Impact Simulation

A frontal Kroell-type chest impact test was simulated with 4.3 m/s impact velocity (Kroell et al., 1974). This impact simulates the blunt impact to the steering wheel in the driver position (see Appendix C for graphical representation of the test). The risk of aortic rupture for this impact velocity is mild to moderate. Since it has been shown by several investigators that the aorta failure is strain based (e.g., Mohan and Melvin (1983)), the comparison between different models used in this study was primarily based on the deformations and the principal and effective (von Mises) strains. First global measures, including the axial strain in DTA and deformation in the arch were investigated. Based on the global measures, regions of interest for comparing the local tissue strain and stress values were determined. For the local measures, the results of four adjacent shell elements in a region of interest were averaged to minimize the effect of mesh resolution.

One of the main contributing mechanisms to TAR is considered to be the axial stretch (Richens, 2003). As the impactor hits the chest, the heart and the ATA move upward and posteriorly while the DTA is relatively fixed which causes stretching in the Isthmus. In order to investigate this axial stretch, the relative resultant distance of a node at the Isthmus was measured with respect to a node at the Lower-DTA in the medial quadrant (Figure 16-a) and the corresponding strain, ε_a, was evaluated.

Another global deformation that investigated was a bending effect in the Arch that makes the inner arch angle (α) to decrease. This effect is caused by the fact that the heart and ATA move posteriorly more than DTA, which is constrained by the vertebral column.

This difference is the rearward motion makes the Arch to bend. To represent α, three nodes were selected in the inner arch and their angle was calculated (Figure 16-b).

Results

A comparison between the undeformed and defomred states of aorta and global measures ε_a and α are shown in Figure 16. As can be seen, ε_a increases and α decreases. The time histories of these changes for the three different models HM, IHM_L and IHM_{LC} are plotted in Figure 17-a which shows that the majority of aorta deformations occured between 10 ms and 30 ms after the impact. In the inhomogenous models, the decrease in α and the increase in ε_a were both higher. The changes in the peak values, compared to HM, were calculated (Figure 17-b). The peak decreases in α were 15% and 9% for IHM_L and IHM_{LC} respectively and occurred at 16.25 ms after the impact. The peak increases in ε_a were 6% and 11% and happened at 20 ms.

Driven by the observed change in α, the principal strain in the inner curvature of the arch was calculated and showed that it significanlty increases in inhomogenous models (Figure 18-a). Comparison of the peak values showed that they increased 40% and 48% for the IHM_L and IHM_{LC} models as comapred to the HM (Figure 18-b) but they occurred after the peak angle at 26.2 ms after the impact.

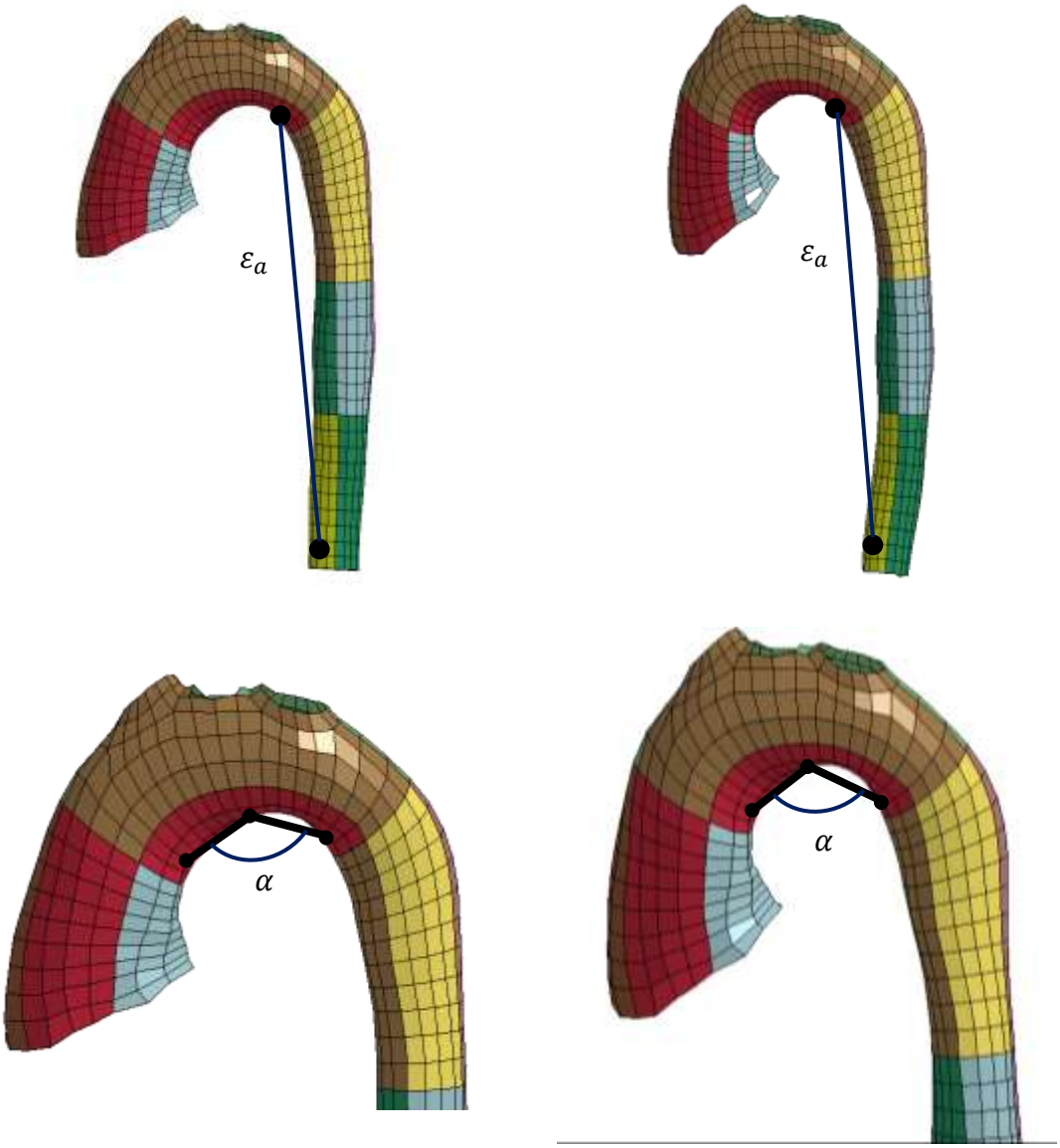

Figure 16– Top) axial strain (ε_a) and b) arch angle (α) in undeformed (left) and deformed (right) states

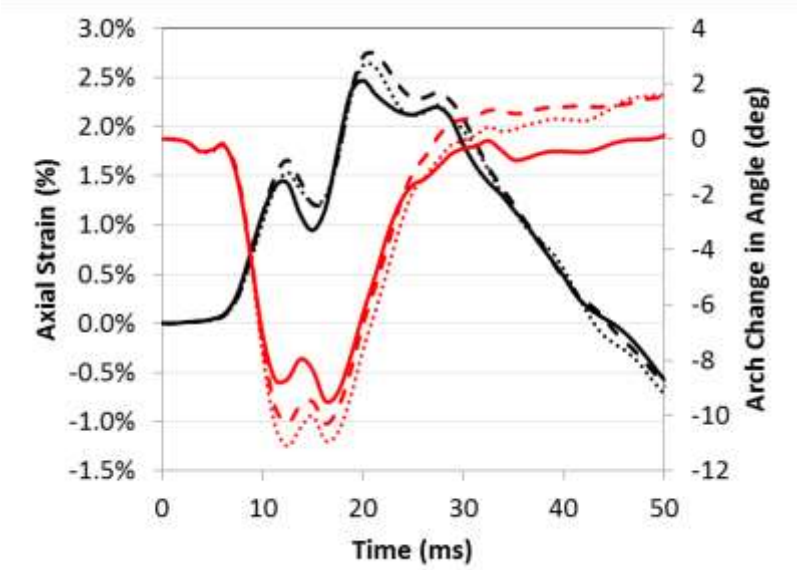

HM IHM$_L$ IHM$_{LC}$ (a)

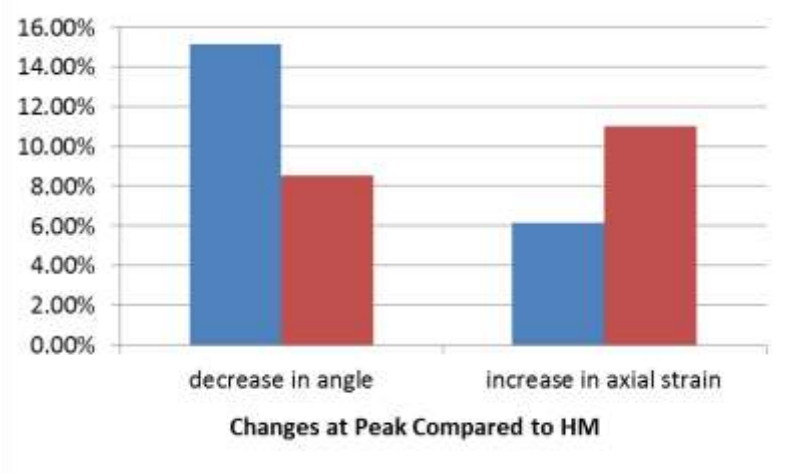

IHM$_L$ IHM$_{LC}$ (b)

Figure 17– a) Time histories of DTA axial strain (ε_a) (black) and change in the arch angle (α) (red). b) Changes in peak α and ε_a in IHM$_L$ and IHM$_{LC}$ relative to HM that occurred at 16.5 ms and 20.0 ms respectively.

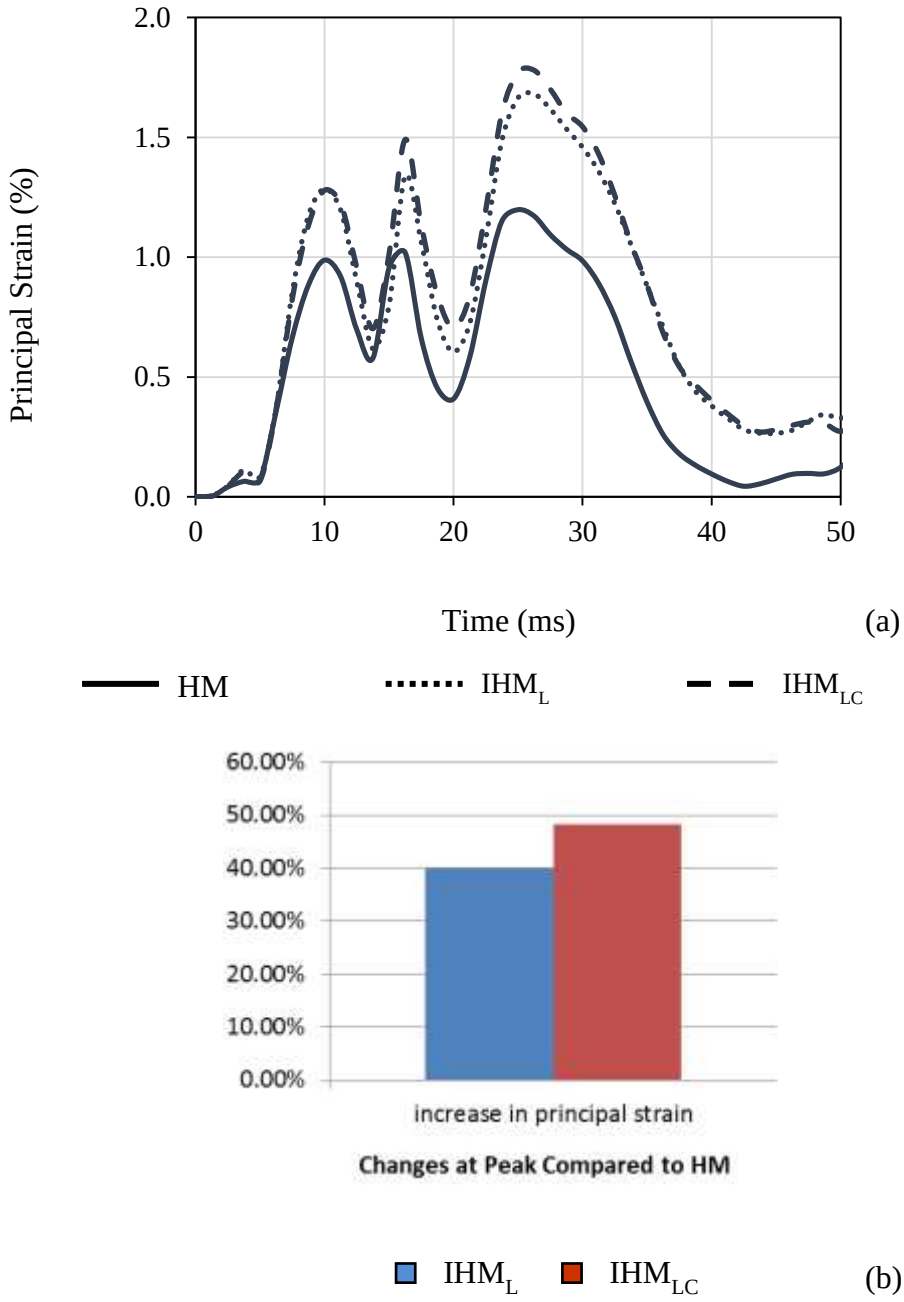

Figure 18– a) Time History of the principal strain at the inner curvature of aortic arch. b) Increase in the peak principal strain as compared to HM that occurred at 26.2 ms.

The percentage of changes in the effective strain in different quadrants and sections in IHM_L and IHM_{LC} as compared to HM are summarized Table 7. The model results that show a higher increase are indicated with the red color. As can be seen, due to inhomogeneity, changes more than 30% were predicted in Isthmus, Arch, and ATA. The values of strains in these sections were compared in more detail (Figure 19) and it was found that the medial quadrant at Isthmus and the posterior quadrant at ATA would be at the highest risk of injury.

The shear relaxation functions used in VE0.05 and VE0.20 models are shown in Figure 20, which indicates that their behavior within the first 50 ms after relaxation are significantly different. The percentage of change in peak effective strain predicted by the viscoelastic model are summarized in Table 8 and shows that the viscoelastic effect primarily affetced the Upper-DTA. The higher decay rate caused strain to increase more than 40% in the medial and lateral quadrants. With respect to the global measures and principal strains, there was about 12% decrease in α, 4% increase in ε_a, and 65% increase in the principal strain at the inner curvature of aortic arch.

Table 7– Percentage of change in the effective strain in IHM_L and IHM_{LC} as compared to HM. Red color indicates the higher increase in strain in each quadrant and green cells indciate the highest increase in each case.

		Effective Strain	
		IHM_L	IHM_{LC}
Lower-DTA	*ANT*	-4.3	-0.1
	LAT	-5.9	-5.0
	MED	-4.0	8.5
	POST	-4.0	-9.1
Mid-DTA	*ANT*	10.8	20.8
	LAT	18.7	20.4
	MED	12.7	23.6
	POST	7.4	14.0
Upper-DTA	*ANT*	6.2	22.8
	LAT	19.8	28.6
	MED	-3.9	6.0
	POST	4.6	12.3
Isthmus	*ANT*	10.9	11.0
	LAT	30.6	11.4
	MED	18.0	-1.6
	POST	27.4	14.5
Arch	*ANT*	21.0	18.9
	LAT	13.9	4.0
	MED	15.0	-6.0
	POST	32.0	15.4
ATA	*ANT*	19.7	6.3
	LAT	9.1	8.1
	MED	10.5	49.5
	POST	17.0	33.0

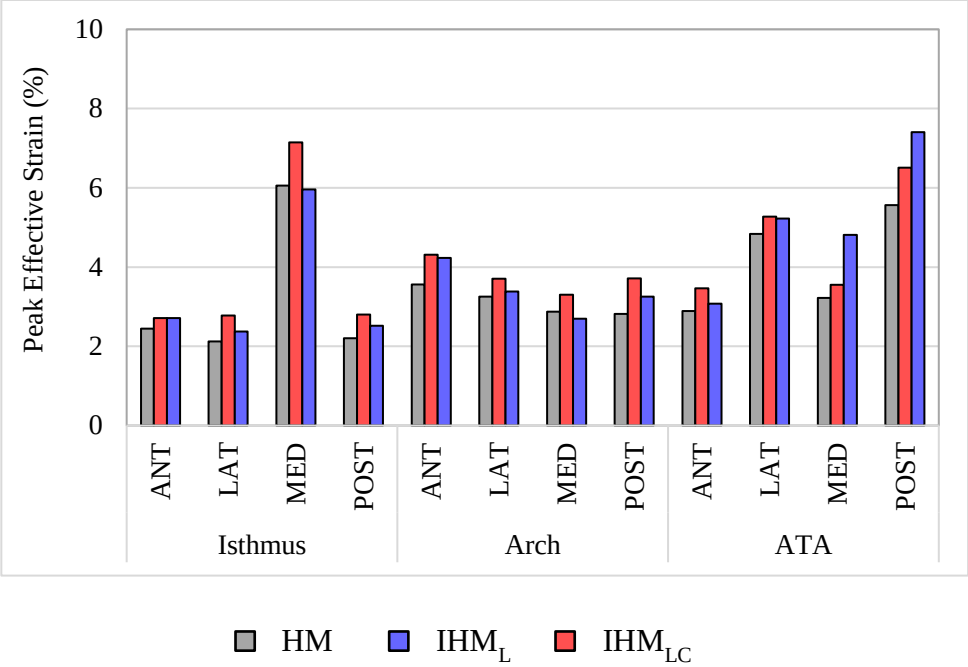

Figure 19– Peak effective strain at various quadrants at Isthmus, Arch, and ATA in HM, IHM$_L$, IHM$_{LC}$ models.

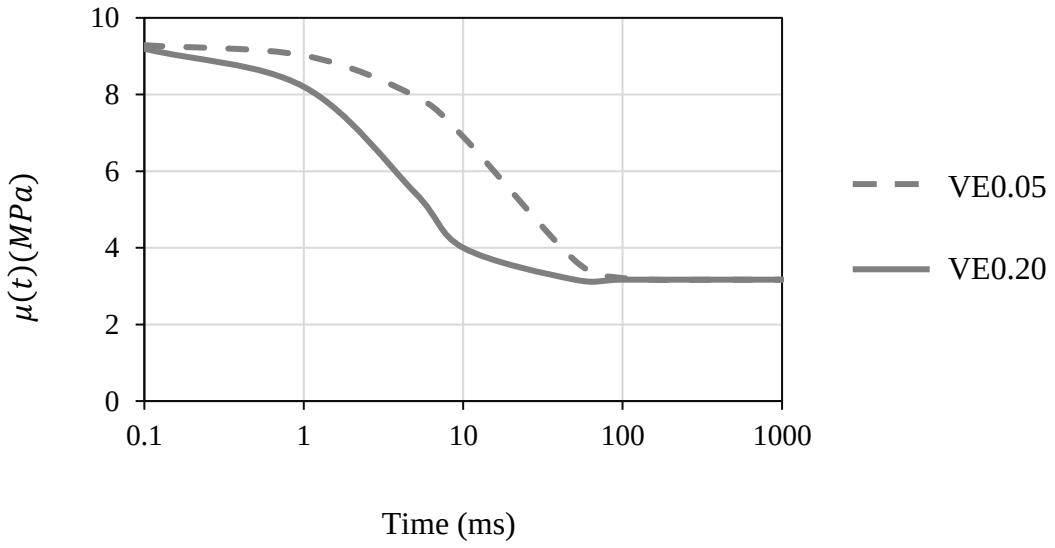

Figure 20– Shear relaxation function of the viscoelastic model (Equation 4.1)

Table 8– Percentage of change in peak effective strain predicted by VE0.20 as compared to VE0.05. Red color indicates the higher increase in strain in each quadrant and the green cell indciate the highest increase.

	Lower-DTA	**Mid-DTA**	**Upper-DTA**	**Isthmus**	**Arch**	**ATA**
ANT	35.3	17.6	18.9	10.8	10.3	12.9
LAT	12.9	20.4	64.5	11.9	6.1	5.4
MED	13.4	16.2	47.9	11.9	10.2	6.2
POST	12.3	22.2	28.8	-1.2	15.4	12.9

Discussion

The results of this study showed that the inhomogeneity and viscoelasticity that were characterized in previous chapters can drastically affect the results of FE models of aorta in chest trauma simulations. Based on inhomogeneity, it was predicted that the aorta would stretch more and the arch would bend more. The viscoelastic model showed that strains may increase significantly based on the prediction of the decay rate. Both of these observations demonstrated that it is imperative to use accurate material models for aorta that address features like inhomogeneity and rate dependency with sufficient accuracy in FE models of TAR.

The FE simulations showed that regions of high risk of rupture, i.e., the medial quadrant of Isthmus and the posterior quadrant of ATA are more sensitive to material inhomogeneity than other regions. Similarly, the decay rate was dramatically affecting the high risk region of Upper-DTA more than others. This means that, using accurate material

properties for aorta is necessary for assessing the risk of injury and designing better injury prevention systems.

The aorta strain levels obtained in this study were generally much lower than the 25% threshold of rupture proposed by other investigators (Shah et al., 2006). This agrees with the fact that a 4.3 m/s Kroell-type is associated with a mild to moderate risk of aortic rupture. Additionally, in the GHBMC model, as most other FE models of human body, the soft tissues are considered stiffer than the reported values in the literature for the purpose of numerical stability. The main purpose of these models so far has been in modeling the global motion of human body and bone fracture in the crash simulations. As a result, it is expected that aorta strains would be less than the real world for identical loading conditions.

It is currently not practical to use a more accurate geometry for aorta that includes the wall thickness and physical material properties. Implementing these features would make the model to be prohibitively large and computationally costly. One solution is to use the results of a model like the GHBMC FBM as the boundary and initial conditions for a more detailed model of only aorta and the immediate surrounding tissues. This approach has its limitations too as many of the tissues material properties are not known yet.

In current GHBMC model, the material properties of other major vessels such as left pulmonary artery, superior vena cava, carotid and subclavian arteries are the same as aorta which is overly simplified. The difference between the material properties of arteries and veins have been demonstrated in the literature (Kamenskiy et al., 2014). Additionally, blood is modeled as an elastic fluid model which is good for simulation of immediate

pressure rise but wouldn't allow the fluid to move and the aorta wall to collapse. More advanced fluid-structure interaction (FSI) algorithms in detailed models of aorta including the Arbitrary Lagrangian Eulerian (ALE) formulation or the Smooth Particle Hydrodynamics (SPH) method.

The material model used for aorta did not include failure. Currently, no validated failure model exists for aorta. Since the effects of inhomogeneity and rate dependence were shown to be significant in the FE model of TAR, it is crucial to characterize these features of the material to the failure point and include them in a FE failure model. It is also important to improve the characterization of these features by increasing the sample size and including the age effect that would reflect the variations in human populations.

CHAPTER 5

CONCLUDING REMARKS

While vehicle safety devices, such as airbags and seat belts, are used more extensively compared to the past, there are still high incidences of TAR in car crashes. Consequently, it is imperative to develop better models for aorta injury/failure prediction that, in turn, can be used to improve the injury prevention systems in cars. The knowledge of aortic mechanical behavior under large deformations and high loading rates is essential to model TAR with FE models. The results of this dissertation advance our understanding of the biomechanics of aorta for application in TAR.

The harmonic inputs approach was expanded to two dimensions, which enabled finding the viscoelastic decay rates and the nonlinearity of the elastic function directly from the experimental data without the need for curve fitting. With this method, decay rates that were 10 to 100 folds higher than previously reported values were obtained. Although, there is usually a large variability in the material properties of biological tissues, the decays rates found in this study were almost consistent. This indicated that the mechanism of rate dependency at high loading rates may be universal and age-independent. The obtained reduced relaxation functions exhibited significant rate dependence within 10 ms of the loading. This is of critical importance in computational modeling of TAR as the rupture occurs typically within 20 ms. A second-order nonlinearity was demonstrated to be applicable to aorta and was implemented in an explicit biaxial relationship between stresses and strains which can be easily implemented in finite element models of TAR. It was shown

that the obtained instantaneous elastic models are within the dynamic biaxial tests results reported previously.

The inhomogeneous and anisotropic mechanical properties of porcine descending thoracic aorta were characterized using nano-indentation tests conducted in axial, circumferential, and radial orientations with about 100 μm spatial resolution. The comparison of $E(t)$ showed that the circumferential direction is stiffer than the axial direction and this difference was more pronounced in the distal sections, and at the lateral quadrant, and in the inner radial layer. Due to the fact that the effects of the residual stresses were ignored in calculating E_C, it is possible that the anisotropic ratio between E_C and E_A using this test method was underestimated.

The elastic moduli increased from proximal to distal sections in all three indentation orientations which is consistent with previous studies. This change can be associated primarily with the collagen content and their undulation. The medial quadrant in axial indentation was found to be significantly more compliant compared to the other quadrants.

Four distinct layers were distinguishable based on the variations of the elastic moduli across the aortic thickness. The outermost layer was significantly more compliant than the other layers was associated with the adventitia. Two radial locations showed relatively higher stiffness, which were attributed to the elastic lamina interna and externa. The medial layer was divided into two sub-layers, with the outer half being stiffer. This increase in the stiffness of the media from the inner layers toward the outer ones has been shown previously to be strongly related to the wall morphological quantities. The results predict that under equal stresses, the inner layers of the medial quadrant in upper DTA

would undergo more strains and would be therefore more prone to failure. This prediction is in agreement with clinical observations.

The simulations with the GHBMC FBM showed that including the inhomogeneity and rate dependence of aorta significantly affect the strain levels measured in aorta during blunt chest impact tests. The risk of injury was changed more dramatically in the Isthmus, Arch, and ATA regions which sustain more strains even in the homogenous model. The global measures of deformations showed that an inhomogeneous aorta and with larger viscoelastic decay rate would undergo more axial strain and arch bending. The local measures, including the principal strains in the inner curvature of the arch and the medial side of upper-DTA showed that due to inhomogeneity the strain can rise up to 50% and due to rate dependency up to 65%.

Limitations and suggestions for Future Research

- In analyzing the biaxial tests a QLV model was used. Developing a fully nonlinear viscoelastic model with multiple hereditary integrals can provide a more accurate estimate of the tissue viscoelastic response. For this purpose, summation of multiple sinusoidal with different frequencies needs to be applied in each direction.
- The constitutive models used in this study are phenomenological. Investigating the correlations between the microscopic structure and the macroscopic biomechanical response of aorta can provide better insights into its mechanisms of deformation, force transmission, and failure. This can be achieved by characterizing the biomechanical properties of aortic microstructure, e.g., collagen and elastin fibers' orientations and their variations with the anatomical location and assessing their contributions to the overall tissue biomechanical properties.
- The porcine aortic tissue is used as a surrogate for healthy human aorta. The nano-indentation methodology presented can be applied to human aortic tissue to characterize the effects of aging and diseases such as atherosclerosis. This can help to better understand the pathogenesis and progression of diseases and developing treatment strategies.
- In current human FE models, including the GHBMC model, the aorta is highly simplified. Developing more detailed and biofidelic finite element models for chest blunt trauma applications rely on implementing more accurate material models that are representative of the biomechanical features of aorta. This can be achieved by accounting for properties such as nonlinearity, anisotropy, inhomogeneity, and wall

thickness. It is also critical to account for the blood flow and its interaction with the vessel wall, e.g., using the Eulerian/Lagrangian approach, in order to investigate the role of pressure rise in the occurrence of TAR.

BIBLIOGRAPHY

Alagona, P., Ahmad, T.A., 2015. Cardiovascular Disease Risk Assessment and Prevention: Current Guidelines and Limitations. Med. Clin. North Am. 99, 711–731. doi:10.1016/j.mcna.2015.02.003

Bass, C.R., Darvish, K., Bush, B., Crandall, J.R., Srinivasan, S.C.M., Tribble, C., Fiser, S., Tourret, L., Evans, J.C., Patrie, J., Wang, C., 2001. Material Properties for Modeling Traumatic Aortic Rupture. Stapp Car Crash J. 45.

Belwadi, A., Siegel, J.H., Singh, A., Smith, J. a, Yang, K.H., King, A.I., 2012. Finite element aortic injury reconstruction of near side lateral impacts using real world crash data. J. Biomech. Eng. 134, 011006. doi:10.1115/1.4005684

Bertrand, S., Cuny, S., Petit, P., Trosseille, X., Page, Y., Guillemot, H., Drazetic, P., 2008. Traumatic rupture of thoracic aorta in real-world motor vehicle crashes. Traffic Inj. Prev. 9, 153–161. doi:10.1080/15389580701775777

Cavanaugh, J.M., Koh, S., Kaledhonkar, S.L., Hardy, W.N., 2005. An Analysis of Traumatic Rupture of the Aorta in Side Impact Sled Tests 2005. doi:10.4271/2005-01-0304

Choudhury, N., Bouchot, O., Rouleau, L., Tremblay, D., Cartier, R., Butany, J., Mongrain, R., Leask, R.L., 2009. Local mechanical and structural properties of healthy and diseased human ascending aorta tissue. Cardiovasc. Pathol. 18, 83–91. doi:10.1016/j.carpath.2008.01.001

Darvish, K., 2009. Comparison between the dynamic moduli of fully non-linear and quasilinear viscoelastic materials. Int. J. Non. Linear. Mech. 44, 239–243. doi:10.1016/j.ijnonlinmec.2008.11.012

Darvish, K.K., Crandall, J.R., 2001. Nonlinear viscoelastic effects in oscillatory shear deformation of brain tissue. Med. Eng. Phys. 23, 633–645. doi:10.1016/S1350-4533(01)00101-1

Deng, Y.C., Kong, W., Ho, H., 1999. Development of a finite element human thorax model for impact injury studies. SAE Int. Congr. Expo.

Fischer-Cripps, A.C., 2007. Introduction to Contact Mechanics, Introduction to Contact Mechanics, Mechanical Engineering Series. Springer US, Boston, MA. doi:10.1007/978-0-387-68188-7

Fung, Y.C., 1993. Biomechanics: mechanical properties of living tissues.

GHBMC M50 Users Manual, 2011. Global HumanBody Models Consortium.

Ghodsi, H., Darvish, K., 2015. Investigation of mechanisms of viscoelastic behavior of collagen molecule. J. Mech. Behav. Biomed. Mater. 51, 194–204. doi:10.1016/j.jmbbm.2015.07.015

Han, H. a C., Fung, Y.C., 1996. Direct measurement strains in aorta of transverse residual. Am. Physiol. Soc.

Haskett, D., Johnson, G., Zhou, A., Utzinger, U., Vande Geest, J., 2010. Microstructural and biomechanical alterations of the human aorta as a function of age and location. Biomech. Model. Mechanobiol. 9, 725–736. doi:10.1007/s10237-010-0209-7

Hedrick, T., 2008. Software techniques for two-and three-dimensional kinematic measurements of biological and biomimetic systems. Bioinspir. Biomim. 3, 034001. doi:10.1088/1748-3182/3/3/034001

Hemmasizadeh, A., Autieri, M., Darvish, K., 2012. Multilayer material properties of aorta determined from nanoindentation tests. J. Mech. Behav. Biomed. Mater. 15, 199–207. doi:10.1016/j.jmbbm.2012.06.008

Hemmasizadeh, A., Tsamis, A., Cheheltani, R., Assari, S., D'Amore, A., Autieri, M., Kiani, M.F., Pleshko, N., Wagner, W.R., Watkins, S.C., Vorp, D., Darvish, K., 2015. Correlations between transmural mechanical and morphological properties in porcine thoracic descending aorta. J. Mech. Behav. Biomed. Mater. 47, 12–20. doi:10.1016/j.jmbbm.2015.03.004

Holzapfel, G. a, Gasser, T.C., Ogden, R.W., 2000. A new constitutive framework for arterial wall mechanics and a comperative study of material models. J. Elast. 61, 1–48. doi:10.1023/A:1010835316564

Iliopoulos, D.C., Deveja, R.P., Kritharis, E.P., Perrea, D., Sionis, G.D., Toutouzas, K., Stefanadis, C., Sokolis, D.P., 2009. Regional and directional variations in the mechanical properties of ascending thoracic aortic aneurysms. Med. Eng. Phys. 31, 1–9. doi:10.1016/j.medengphy.2008.03.002

Kamenskiy, A. V, Dzenis, Y.A., Kazmi, S.A.J., Pemberton, M.A., Pipinos, I.I., Phillips, N.Y., Herber, K., Woodford, T., Bowen, R.E., Lomneth, C.S., MacTaggart, J.N.,

2014. Biaxial mechanical properties of the human thoracic and abdominal aorta, common carotid, subclavian, renal and common iliac arteries. Biomech. Model. Mechanobiol. 13, 1341–59. doi:10.1007/s10237-014-0576-6

Kim, J., Baek, S., 2011. Circumferential variations of mechanical behavior of the porcine thoracic aorta during the inflation test. J. Biomech. 44, 1941–1947. doi:10.1016/j.jbiomech.2011.04.022

Kim, J.-H., Avril, S., Duprey, A., Favre, J.-P., 2012. Experimental characterization of rupture in human aortic aneurysms using a full-field measurement technique. Biomech. Model. Mechanobiol. 11, 841–853. doi:10.1007/s10237-011-0356-5

Kroell, C.K., Schneider, D.C., Nahum, A.M., 1974. Impact tolerance and response of the human Thorax II, in: Proc. 18th Stapp Car Crash Conference. pp. 383–457.

Lai, W.M., Rubin, D., Krempl, E., 2004. Introduction to Continuum Mechanics.

Lillie, M.A., Shadwick, R.E., Gosline, J.M., 2010. Mechanical anisotropy of inflated elastic tissue from the pig aorta. J. Biomech. 43, 2070–2078. doi:10.1016/j.jbiomech.2010.04.014

Marra, S.P., Kennedy, F.E., Kinkaid, J.N., Fillinger, M.F., 2006. Elastic and rupture properties of porcine aortic tissue measured using inflation testing. Cardiovasc. Eng. 6, 123–131. doi:10.1007/s10558-006-9021-5

Mills, S.E., 2007. Histology for pathologists, 3rd ed. Lippincott Williams & Wilkins.

Mohan, D., Melvin, J.W., 1983. Failure properties of passive human aortic tissue. II—Biaxial tension tests. J. Biomech. 16, 31–44. doi:10.1016/0021-9290(83)90044-1

Mohan, D., Melvin, J.W., 1982. Failure properties of passive human aortic tissue. I--uniaxial tension tests. J. Biomech. 15, 887–902. doi:10.1016/0021-9290(83)90044-1

National Instruments, 1998.

Oie, T., Murayama, Y., Fukuda, T., Nagai, C., Omata, S., Kanda, K., Yaku, H., Nakayama, Y., 2009. Local elasticity imaging of vascular tissues using a tactile mapping system. J. Artif. Organs 12, 40–46. doi:10.1007/s10047-008-0440-5

Pena, J.A., Martinez, M.A., Pe??a, E., 2015. Layer-specific residual deformations and uniaxial and biaxial mechanical properties of thoracic porcine aorta. J. Mech. Behav. Biomed. Mater. 50, 55–69. doi:10.1016/j.jmbbm.2015.05.024

Plummer, D., Petro, K., Akbari, C., O'Donnell, S., 2006. Endovascular repair of traumatic thoracic aortic disruption. Perspect. Vasc. Surg. Endovasc. Ther. 18, 132–9. doi:10.1177/1531003506293453

Popov, E., 1990. Engineering Mechanics of Solids. Prentice Hall.

Purslow, P.P., 1983. Positional variations in fracture toughness, stiffness and strength of descending thoracic pig aorta. J. Biomech. 16, 947–953. doi:10.1016/0021-9290(83)90058-1

Raghavan, M.L., Vorp, D.A., Federle, M.P., Makaroun, S., Webster, M.W., 2000. Wall stress distribution on three- dimensionally reconstructed models of human abdominal aortic aneurysm. J. Vasc. Surg. 31, 760–769. doi:10.1067/mva.2000.103971

Rastgar-Agah, M., Laksari, K., Assari, S., Darvish, K., 2016. Mechanical Instability of Aorta due to Intraluminal Pressure. Int. J. Appl. Mech. 08, 1650002. doi:10.1142/S1758825116500022

Richens, D., 2003. Rupture of the aorta following road traffic accidents in the United Kingdom 1992–1999. The results of the co-operative crash injury study. Eur. J. Cardio-Thoracic Surg. 23, 143–148. doi:10.1016/S1010-7940(02)00720-0

Richens, D., Field, M., Hashim, S., Neale, M., Oakley, C., 2004. A finite element model of blunt traumatic aortic rupture. Eur. J. Cardio-thoracic Surg. 25, 1039–1047. doi:10.1016/j.ejcts.2004.01.059

Richens, D., Field, M., Neale, M., Oakley, C., 2002. The mechanism of injury in blunt traumatic rupture of the aorta. Eur. J. Cardio-thoracic Surg. 21, 288–293. doi:10.1016/S1010-7940(01)01095-8

Roveri, N., Ripamonti, A., Pulga, C., Ciamician, I.C.G., Bologna, U., Jeronimidb, G., Purslow, P.P., Voipin, D., Gotte, L., Istologia, I., Padova, U., 1979. Mechanical Behaviour of Aortic Tissue as a Function of Collagen Orientation. Makromol. Chem. 181, 1999–2007.

Ryb, G.E., Dischinger, P.C., Kleinberger, M., McGwin, G., Griffin, R.L., 2013. Aortic injuries in newer vehicles. Accid. Anal. Prev. 59, 253–259. doi:10.1016/j.aap.2013.06.007

Schriefl, A.J., Zeindlinger, G., Pierce, D.M., Regitnig, P., Holzapfel, G.A., 2012. Determination of the layer-specific distributed collagen fibre orientations in human thoracic and abdominal aortas and common iliac arteries. J. R. Soc. Interface 9, 1275–1286. doi:10.1098/rsif.2011.0727

Shah, C.S., Hardy, W.N., Mason, M.J., Yang, K.H., Van Ee, C.A., Morgan, R., Digges, K., 2006. Dynamic biaxial tissue properties of the human cadaver aorta. Stapp Car Crash J.

Shah, C.S., Yang, K.H., Hardy, W., Wang, H.K., King, A.I., 2001. Development of a computer model to predict aortic rupture due to impact loading. Stapp Car Crash J. 45, 161–82.

Sokolis, D.P., Boudoulas, H., Kerayannacos, P.E., 2008. Segmental differences of aortic function and composition: clinical implications. Hellenic J. Cardiol. 49, 145–154.

Sun, W., Sacks, M.S., 2005. Finite element implementation of a generalized Fung-elastic constitutive model for planar soft tissues. Biomech. Model. Mechanobiol. 4, 190–9. doi:10.1007/s10237-005-0075-x

Teixeira, P.G., Inaba, K., Barmparas, G., 2011. Blunt Thoracic Aortic Injuries: An Autopsy Study. J. Vasc. Surg. 54, 581. doi:10.1016/j.jvs.2011.06.087

Viano, D.C., 1983. Biomechanics of Nonpenetrating Aortic Trauma: A Review. doi:10.4271/831608

Vlassak, J.J., Ciavarella, M., Barber, J.R., Wang, X., 2003. The indentation modulus of elastically anisotropic materials for indenters of arbitrary shape. J. Mech. Phys. Solids 51, 1701–1721. doi:10.1016/S0022-5096(03)00066-8

Vorp, D.A., 2007. Biomechanics of abdominal aortic aneurysm. J. Biomech. 40, 1887–1902. doi:10.1016/j.jbiomech.2006.09.003

Waldman, S.D., Michael Lee, J., 2002. Boundary conditions during biaxial testing of planar connective tissues. Part 2: Fiber Orientation. J. Mater. Sci. Mater. Med. 21, 1215 – 1221. doi:10.1023/A:1019896210320

Wang, J.C., Bennett, M., 2012. Aging and atherosclerosis: Mechanisms, functional consequences, and potential therapeutics for cellular senescence. Circ. Res. 111, 245–259. doi:10.1161/CIRCRESAHA.111.261388

Yuen, K.F., 2009. Development of a human body model for the analysis of side impact automotive thoracic trauma. University of Waterloo, Canada.

Zeinali-Davarani, S., Wang, Y., Chow, M.-J., Turcotte, R., Zhang, Y., 2015. Contribution of collagen fiber undulation to regional biomechanical properties along porcine thoracic aorta. J. Biomech. Eng. 137, 051001. doi:10.1115/1.4029637

APPENDIX A

BIAXIAL TESTS OPTIMIZATION CONSTRAINTS

When optimizing for the material coefficients, one may find more than one possible set of material coefficients that would predict the material behavior equally well. In order to make sure that the constitutive model is physically meaningful and numerically stable, two restrictions were applied: the convexity of the strain energy function, and the condition number of material stiffness matrix set lower than a prescribed value (Holzapfel et al., 2000; Sun and Sacks, 2005).

The convexity of the strain energy function is guaranteed by making sure that its second derivative with respect to E is positive definite. This means that an increase in either tensile or compressive strain would result in an increase in internal energy.

$$\frac{\partial^2 W}{\partial \mathbf{F} \partial \mathbf{F}} \geq 0 \tag{A.1}$$

The condition number of $\boldsymbol{C}$ is defined as:

$$k(\boldsymbol{C}) = \left(\frac{\lambda_{max}(\mathbf{A})}{\lambda_{min}(\mathbf{A})} \right)^{\frac{1}{2}} \tag{A.2}$$

where $\mathbf{A} = \boldsymbol{C}'\boldsymbol{C}$ and λ_{max} and $\lambda_{min}$are the maximum and minimum eigenvalues of $\mathbf{A}$. The lower values of k ensures the numerical stability.

DERIVATION OF DEFORMATION GRADIENT TENSOR

The pure biaxial deformation, i.e., no shear deformation, is considered as:

$$x_1 = \lambda_1 X_1 \; ; \qquad x_2 = \lambda_2 X_2 \tag{A.3}$$

where X_i and x_i are the spatial (reference) and material (deformed) coordinates, respectively, and λ_i are the stretch ratios. We assume that for three vertices of a triangular element, *p*, *q*, and *r*, the distances are known in the deformed state ($\overline{pq}$ and $\overline{pr}$) and their corresponding coordinates are known in the reference state (P_1, P_2, and so on). $\overline{pq}$ and $\overline{pr}$ can be written as:

$$\begin{aligned} \overline{pq}^2 &= (p_1 - q_1)^2 + (p_2 - q_2)^2 \\ &= (\lambda_1(P_1 - Q_1))^2 + (\lambda_2(P_2 - Q_2))^2 \\ \overline{pr}^2 &= (p_1 - r_1)^2 + (p_2 - r_2)^2 \\ &= (\lambda_1(P_1 - R_1))^2 + (\lambda_2(P_2 - R_2))^2 \end{aligned} \tag{A.4}$$

which is equivalent to:

$$\begin{bmatrix} \lambda_1^2 \\ \lambda_2^2 \end{bmatrix} = \begin{bmatrix} (P_1 - Q_1)^2 & (P_2 - Q_2)^2 \\ (P_1 - R_1)^2 & (P_2 - R_2)^2 \end{bmatrix}^{-1} \begin{bmatrix} \overline{pq}^2 \\ \overline{pr}^2 \end{bmatrix} \tag{A.5}$$

APPENDIX B

DETAILED RESULTS OF NANO-INDENTATION TESTS

Table 9 – Elastic moduli at different relaxation times grouped by section, quadrant, and layer for a) Axial, b) Circumferential, and c) Radial indentations

a) Axial Indentation													
		E_0 **(kPa)**		E**(0.01) (kPa)**		E**(0.1) (kPa)**		E**(1) (kPa)**		E**(10) (kPa)**		E**(∞) (kPa)**	
i) Effect of *r* by *z*-direction													
Upper-DTA	**Layer I**	123.01	(38.57)	87.03	(28.60)	61.43	(22.13)	51.42	(19.24)	41.76	(16.89)	38.14	(16.35)
	Layer II	119.23	(33.67)	84.37	(25.29)	59.34	(19.63)	49.74	(17.35)	41.38	(15.61)	38.49	(15.22)
	Layer III	120.07	(32.73)	84.20	(24.93)	59.02	(19.83)	49.69	(18.06)	41.35	(16.43)	38.51	(15.94)
	Layer IV	88.61	(32.05)	60.36	(24.43)	40.45	(18.54)	32.57	(15.68)	26.06	(13.07)	24.14	(12.09)
Mid-DTA	**Layer I**	122.07	(34.92)	85.77	(24.54)	59.87	(17.99)	49.55	(15.71)	40.42	(13.56)	37.34	(12.86)
	Layer II	104.82	(30.36)	72.79	(21.80)	49.55	(16.00)	40.60	(13.63)	33.38	(11.42)	31.05	(10.68)
	Layer III	117.09	(41.15)	81.06	(28.65)	55.51	(20.26)	46.01	(17.03)	37.98	(13.95)	35.37	(12.89)
	Layer IV	95.94	(27.32)	65.86	(19.58)	44.70	(14.65)	36.69	(13.11)	29.91	(11.47)	27.79	(10.88)
Lower-DTA	**Layer I**	127.29	(41.50)	89.21	(29.66)	61.94	(21.87)	51.09	(18.81)	41.19	(16.11)	37.69	(15.27)
	Layer II	130.01	(45.41)	90.11	(32.18)	61.46	(23.01)	50.14	(19.27)	40.40	(15.99)	37.14	(14.91)
	Layer III	135.93	(44.76)	94.75	(31.46)	65.65	(22.45)	54.27	(18.92)	44.00	(15.85)	40.52	(14.85)

(cont.)

a) Axial Indentation													
		E_0 (kPa)		E(0.01) (kPa)		E(0.1) (kPa)		E(1) (kPa)		E(10) (kPa)		E(∞) (kPa)	
ii) Effect of θ by *z*-direction													
Upper-DTA	**LAT**	116.39	(36.45)	81.64	(27.67)	56.98	(21.51)	47.52	(18.94)	39.33	(16.69)	36.61	(15.96)
	MED	120.89	(31.70)	85.46	(23.64)	60.30	(18.66)	50.82	(16.90)	42.07	(15.55)	38.88	(15.36)
Mid-DTA	**ANT**	110.86	(33.13)	77.82	(23.43)	54.27	(17.02)	45.09	(14.68)	37.10	(12.31)	34.42	(11.47)
	LAT	122.37	(38.62)	84.98	(26.89)	58.26	(19.32)	48.17	(16.53)	39.78	(13.80)	37.04	(12.85)
	MED	103.03	(28.20)	71.28	(20.21)	48.48	(15.00)	39.87	(13.02)	32.80	(11.17)	30.51	(10.58)
	POST	112.65	(44.52)	77.73	(31.40)	52.80	(22.28)	43.19	(18.43)	35.17	(14.84)	32.61	(13.61)
Lower-DTA	**ANT**	151.44	(41.46)	103.49	(29.45)	69.86	(21.13)	57.11	(17.63)	46.00	(14.74)	42.41	(13.8)
	LAT	137.96	(41.58)	97.05	(29.73)	67.60	(21.53)	55.80	(18.24)	45.43	(15.48)	41.90	(14.62)
	MED	107.49	(29.96)	75.29	(22.11)	52.27	(16.86)	42.97	(14.51)	34.49	(12.14)	31.54	(11.34)
	POST	156.20	(55.13)	107.82	(38.82)	73.65	(27.91)	60.69	(23.61)	49.11	(19.58)	45.15	(18.17)
iii) Effect of *r* by θ-direction													
ANT	**Layer I**	130.13	(38.47)	91.30	(27.22)	63.87	(20.26)	53.26	(17.84)	43.87	(15.81)	40.74	(15.24)
	Layer II	128.72	(42.97)	89.85	(29.73)	62.05	(20.69)	51.21	(17.13)	41.89	(13.88)	38.79	(12.77)
	Layer III	120.33	(38.84)	82.99	(26.49)	56.70	(18.30)	46.70	(15.29)	37.94	(12.39)	35.06	(11.39)
	Layer IV	92.90	(24.99)	64.30	(17.71)	44.34	(12.76)	36.65	(10.96)	29.79	(9.30)	27.55	(8.75)
LAT	**Layer I**	132.31	(36.57)	92.92	(26.52)	64.73	(19.99)	53.58	(17.49)	43.71	(15.10)	40.34	(14.26)
	Layer II	119.54	(37.57)	83.83	(27.88)	57.91	(21.04)	47.76	(18.06)	39.44	(15.41)	36.72	(14.52)
	Layer III	131.29	(41.95)	91.40	(29.04)	63.10	(20.51)	52.37	(17.29)	43.04	(14.41)	39.91	(13.51)
	Layer IV	102.19	(37.14)	70.42	(27.39)	48.27	(20.79)	39.86	(18.52)	32.78	(16.21)	30.66	(15.34)
MED	**Layer I**	108.37	(31.31)	76.62	(22.84)	53.79	(17.32)	44.48	(14.83)	35.76	(12.63)	32.59	(12.04)
	Layer II	100.51	(25.00)	69.64	(18.00)	47.20	(13.39)	38.49	(11.49)	31.23	(9.75)	28.78	(9.25)
	Layer III	113.66	(32.27)	79.36	(23.77)	55.15	(18.20)	46.04	(16.06)	38.06	(13.99)	35.39	(13.29)
	Layer IV	91.57	(22.72)	62.18	(16.75)	41.00	(12.99)	32.87	(11.77)	26.45	(10.30)	24.47	(9.70)
POST	**Layer I**	130.59	(40.71)	91.05	(27.89)	62.89	(19.82)	51.79	(17.21)	41.82	(14.45)	38.39	(13.43)
	Layer II	115.71	(45.06)	79.27	(31.17)	53.26	(21.76)	43.42	(18.12)	35.31	(14.79)	32.72	(13.68)
	Layer III	134.99	(59.74)	93.40	(42.34)	63.90	(30.16)	52.59	(25.00)	42.82	(20.13)	39.61	(18.42)
	Layer IV	87.69	(19.84)	59.21	(12.52)	39.14	(7.86)	31.61	(6.23)	25.39	(4.51)	23.48	(3.96)

b) Circumferential Indentation													
		E_0 (kPa)		E(0.01) (kPa)		E(0.1) (kPa)		E(1) (kPa)		E(10) (kPa)		E(∞) (kPa)	
i) Effect of *r* by *z*-direction													
Upper-DTA	**Layer I**	139.77	(48.59)	97.27	(32.91)	68.07	(22.80)	57.03	(19.35)	45.50	(14.11)	41.13	(12.08)
	Layer II	118.96	(40.38)	83.83	(30.47)	59.59	(24.12)	50.48	(21.65)	42.06	(19.12)	39.24	(18.19)
	Layer III	121.36	(39.18)	87.37	(29.89)	62.95	(23.25)	53.01	(20.90)	44.38	(18.62)	41.52	(17.94)
	Layer IV	89.02	(29.63)	62.87	(21.74)	44.48	(16.84)	36.54	(15.14)	28.64	(13.24)	25.84	(12.62)
Mid-DTA	**Layer I**	156.04	(64.34)	107.60	(44.40)	75.47	(31.58)	64.54	(27.39)	53.79	(22.92)	50.19	(21.31)
	Layer II	122.09	(40.42)	85.46	(29.60)	59.92	(22.08)	50.19	(18.72)	41.35	(15.91)	38.40	(15.04)
	Layer III	131.93	(36.83)	93.30	(26.97)	66.67	(20.62)	56.57	(18.12)	47.38	(15.64)	44.41	(14.78)
	Layer IV	122.94	(7.04)	85.78	(9.31)	60.26	(10.85)	50.76	(9.98)	42.26	(9.27)	39.58	(9.02)
Lower-DTA	**Layer I**	166.19	(56.73)	115.67	(40.89)	82.31	(30.99)	71.10	(27.76)	59.99	(24.19)	56.28	(22.90)
	Layer II	133.92	(56.14)	94.86	(41.63)	67.75	(32.40)	57.78	(29.10)	48.81	(25.27)	45.83	(23.85)
	Layer III	142.78	(50.68)	102.10	(36.26)	73.79	(26.80)	62.69	(23.31)	52.54	(19.65)	49.21	(18.38)
ii) Effect of θ by *z*-direction													
Upper-DTA	**LAT**	109.01	(34.62)	77.13	(25.98)	54.72	(20.50)	45.73	(18.23)	37.59	(16.02)	34.90	(15.28)
	MED	134.23	(44.81)	95.49	(32.61)	68.33	(24.39)	57.88	(21.67)	47.99	(18.59)	44.47	(17.65)
Mid-DTA	**LAT**	140.56	(41.53)	99.18	(29.55)	70.48	(21.71)	59.52	(18.64)	49.58	(15.70)	46.32	(14.65)
	MED	123.92	(44.83)	86.32	(31.97)	60.74	(23.81)	51.46	(20.92)	42.77	(18.02)	39.90	(17.09)
Lower-DTA	**LAT**	141.66	(51.27)	100.39	(36.76)	72.28	(27.60)	61.92	(24.52)	52.24	(20.97)	49.07	(19.67)
	MED	144.24	(57.54)	102.36	(42.01)	73.24	(32.08)	62.25	(28.48)	52.26	(24.55)	48.92	(23.15)
iii) Effect of *r* by θ-direction													
LAT	**Layer I**	149.97	(48.65)	103.85	(32.87)	72.92	(22.93)	61.83	(19.93)	51.15	(17.03)	47.65	(16.08)
	Layer II	127.46	(45.70)	89.85	(33.85)	63.76	(26.04)	53.90	(22.92)	45.00	(19.72)	42.09	(18.56)
	Layer III	129.14	(42.71)	92.35	(31.28)	66.68	(23.95)	56.63	(21.26)	47.50	(18.32)	44.50	(17.26)
	Layer IV	90.33	(29.03)	64.78	(22.61)	46.21	(18.07)	37.57	(16.16)	29.55	(14.65)	26.82	(14.25)
MED	**Layer I**	158.02	(64.54)	109.84	(45.74)	77.64	(33.82)	66.62	(29.87)	55.03	(25.05)	50.76	(23.42)
	Layer II	123.60	(48.11)	87.04	(35.79)	61.64	(27.81)	52.21	(24.86)	43.58	(21.83)	40.64	(20.79)
	Layer III	135.60	(44.20)	96.64	(32.27)	69.29	(24.16)	58.57	(21.15)	49.00	(18.26)	45.87	(17.37)
	Layer IV	112.82	(27.67)	77.67	(19.76)	54.16	(15.34)	45.91	(13.55)	37.72	(11.73)	34.91	(11.24)

c) Radial Indentation													
		***E*₀ (kPa)**		***E*(0.01) (kPa)**		***E*(0.1) (kPa)**		***E*(1) (kPa)**		***E*(10) (kPa)**		***E*(∞) (kPa)**	
i) Effect of θ by *z*-direction													
Upper-DTA	**LAT**	142.35	(32.36)	105.61	(24.11)	76.41	(18.32)	59.00	(14.9)	41.32	(11.24)	34.47	(9.86)
	MED	140.48	(41.89)	105.08	(31.70)	77.90	(24.61)	62.83	(21.45)	45.81	(17.59)	38.64	(15.93)
Mid-DTA	**LAT**	169.62	(49.73)	124.46	(33.94)	89.45	(23.56)	69.92	(20.32)	50.42	(17.10)	43.04	(15.98)
	MED	149.31	(21.82)	112.43	(16.49)	82.86	(12.76)	64.48	(11.14)	44.83	(9.06)	36.93	(8.10)
Lower-DTA	**LAT**	179.06	(46.20)	132.60	(32.61)	97.71	(24.63)	79.19	(22.44)	58.21	(19.23)	49.46	(17.75)
	MED	176.71	(39.18)	130.82	(28.65)	95.55	(21.44)	76.16	(18.86)	54.93	(15.87)	46.18	(14.45)

NANO-INDENTATION TEST SETUP

The custom-made nano-indentation setup previously designed in Tissue Biomechanics Laboratory was used in this dissertation and is briefly described below and in Figure 21.

The setup consisted of a Z-axis nano-positioner with 0.2 nm resolution and 100 μm range of motion (Nano-Z100, MCL, WI) combined with a horizontal piezo micro-positioner (M-663.4 PX, PI, MA). A conical indenter (XPT, Agilent Technologies, CA 55° tip angle, 10 μm tip rounding radius) was attached to a force transducer (Model 406A, Aurora Scientific, Ontario, Canada) with resolution of 0.1 μN. The setup is equipped with a 300x stereo microscope (Olympus SZX7) for contact visualization. The test setup was mounted on an active isolation table (TMC 63-533, Peabody, MA).

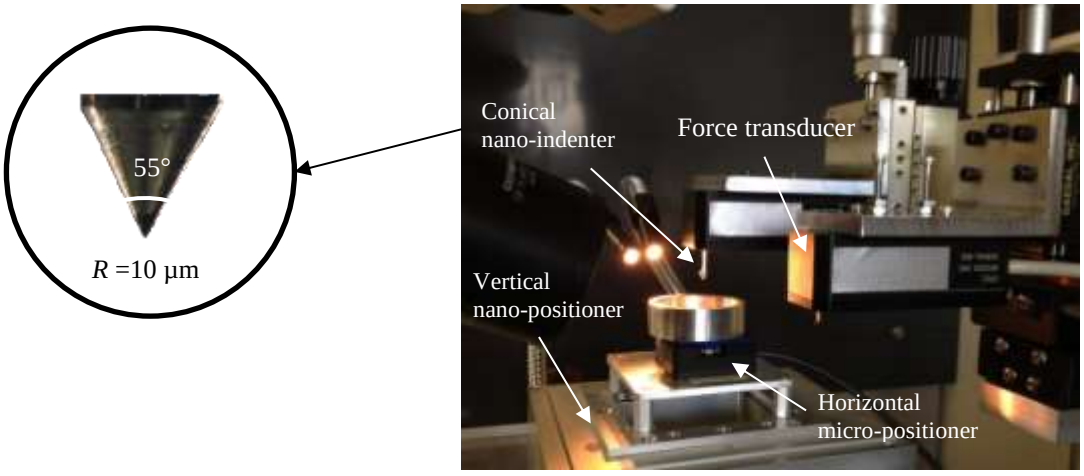

Figure 21 – Experimental setup and conical tip used for nanoindentation on the aortic specimens.

APPENDIX C

GLOBAL HUMAN BODY MODELS CONSORTIUM (GHBMC)

The GHMBC model is a finite element (FE) model developed for simulating the automotive injuries. The GHBMC baseline data, including age, weight, and height, are obtained from a 50th percentile male volunteer with height, weight, and BMI of 174.9 cm, 78.6 ± 0.77 kg, and 25.7 ± 0.25, respectively. The model consists of five Body Region Models (BRM) including the head, neck, thorax, abdomen, and pelvis/lower extremity. The GHBMC thorax model was developed with the objective of predicting specific crash-induced thoracic injuries including rib fracture, lung puncture, and cardiovascular tissue risk of failure. Figure 22 shows the positioning of the GHBMC model in the driver positions, and the chest impact model.

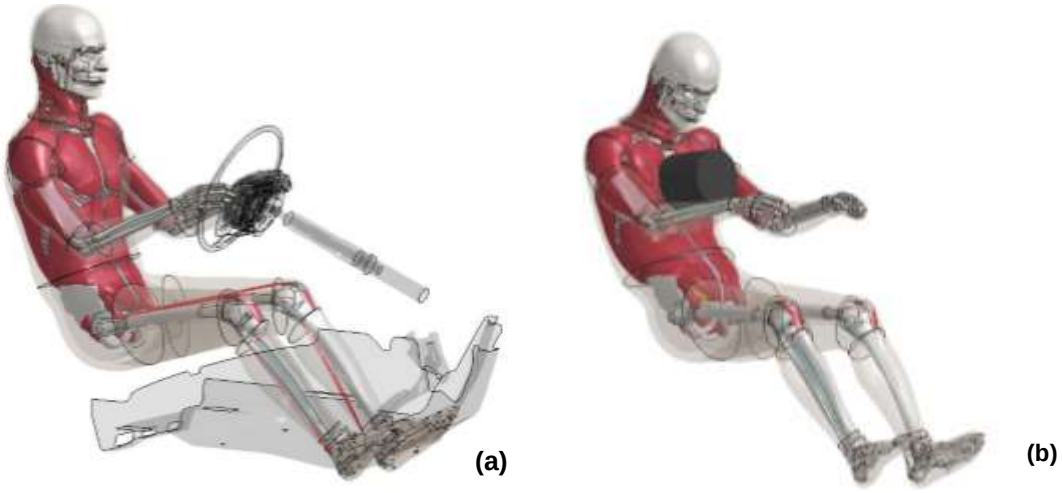

Figure 22 - Positioning of the model in the driver position (a) and chest impact model (b)

The thorax region consists of 0.48 million elements with 2048 elements and 3216 nodes used to create the FE model of heart and aorta. Figure 23 shows the general view of the heart and the aorta which are modeled as shells filled with solid fluids.

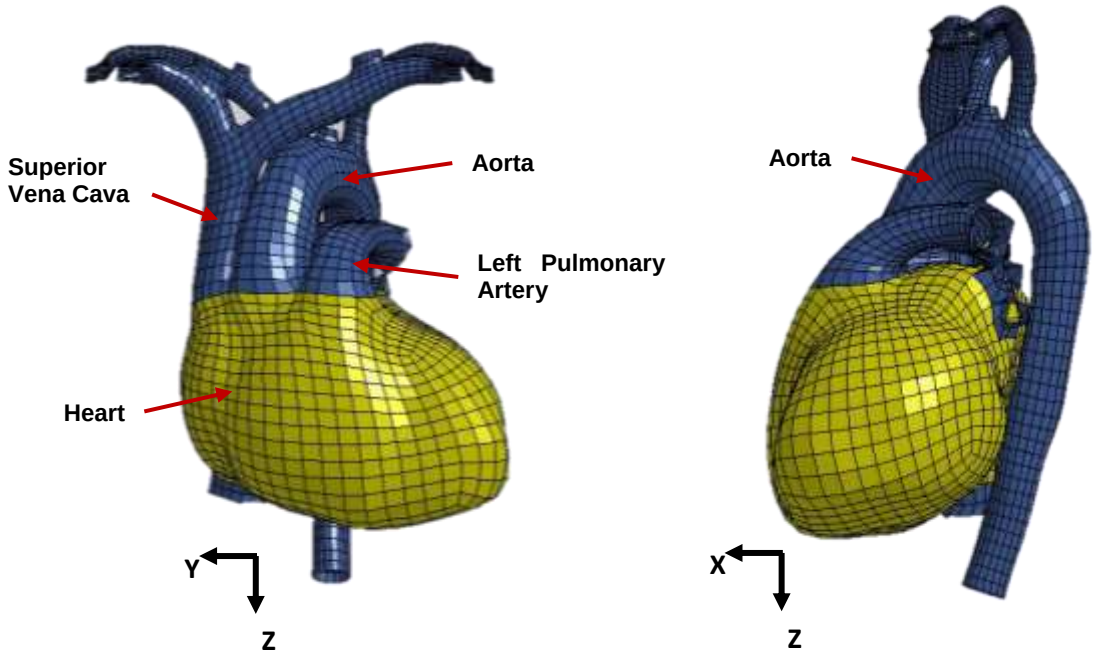

Figure 23 - Frontal and lateral views of heart and aorta in GHBMC

The material models are obtained from LS-DYNA Keyword User's Manual, Volume II.

MAT_ELASTIC (1): This is an isotropic material which can be assigned to beam, shell, and solid elements in LS-DYNA.

MAT_ELASTIC_FLUID (1): The fluid option is valid for solid elements only, where the bulk modulus (K) has to be defined as Young's modulus and Poisson's ratio is ignored and the shear modulus is assumed to be zero.

$$K = \frac{E}{3(1-2v)} \tag{C.1}$$

MAT_HEART_TISSUE (128): This material model is used for heart tissue. The tissue model is described in terms of the energy function based on the Green strain components, E_{ij}.

$$W(E) = \frac{c}{2}(e^{Q} - 1) + \frac{1}{2}\, P\, (I_3 - 1) \tag{C.2}$$

$$Q = B_1 E_{11}^2 + B_2(E_{22}^2 + E_{33}^2 + E_{23}^2 + E_{32}^2) + B_3(E_{12}^2 + E_{21}^2 + E_{13}^2 + E_{31}^2) \tag{C.3}$$

The global deformation of the aorta along with the contour plots of strain are shown in Figure 24. As the impactor hits the chest, the heart and the ATA move upward and posteriorly while the DTA is relatively fixed.

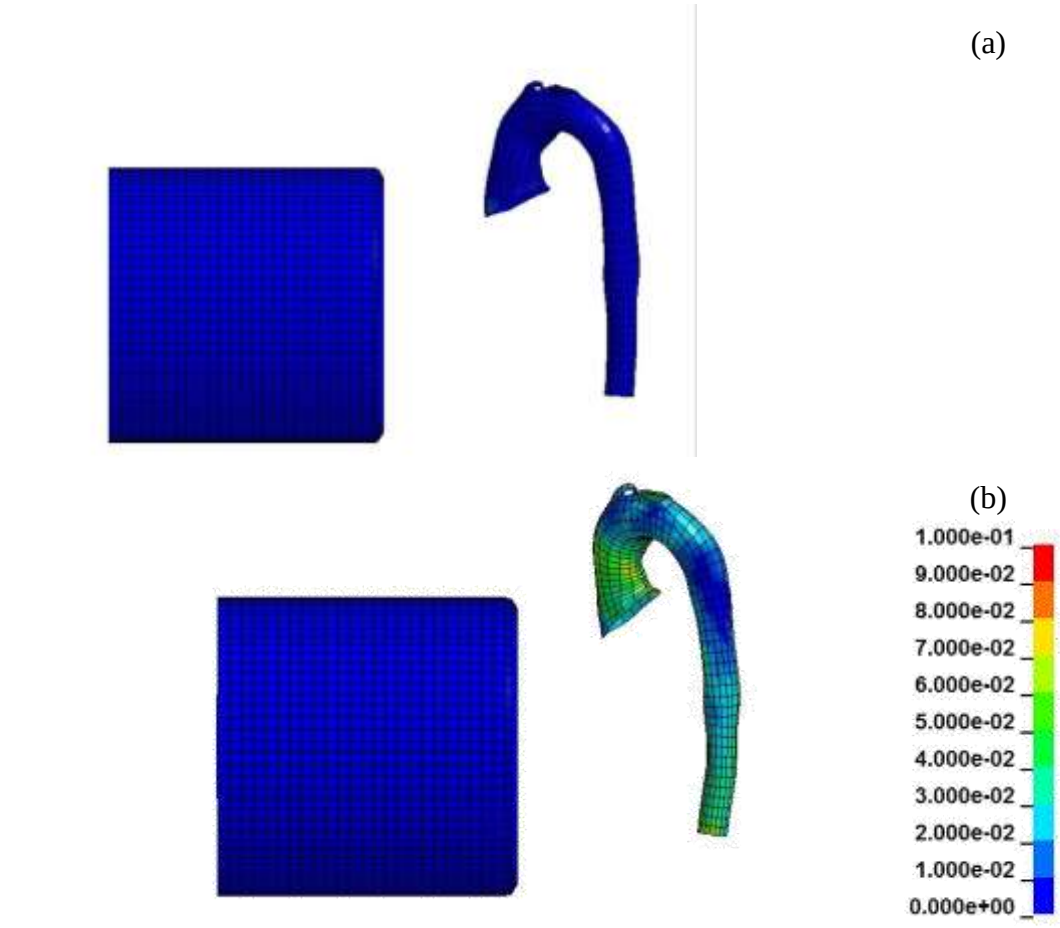

Figure 24– Representative effective strain fringe plots for HM a) before the impactor hits the body, and b) at the state of maximum strain in the aortic Isthmus